On the use of Li isotopes as a proxy for water-rock interaction in fractured crystalline rocks: a case study from the Gotthard rail base tunnel

Christoph Wanner[1*], Kurt Bucher[2], Philip A. E. Pogge von Strandmann[3], H. Niklaus Waber[1], Thomas Pettke[1]

[1]Rock Water Interaction Group, Institute of Geological Sciences, University of Bern, Baltzerstrasse 3, CH-3012 Bern, Switzerland.

[2]Institute of Geosciences, Mineralogy and Geochemistry, University of Freiburg, Germany.

[3]Institute of Earth and Planetary Sciences, University College London and Birkbeck, University of London, UK.

**corresponding author (email: wanner@geo.unibe.ch, phone: +41316314023, fax: +41316314843)*

ABSTRACT

We present Li isotope measurements of groundwater samples collected during drilling of the 57 km long Gotthard rail base tunnel in Switzerland, to explore the use of Li isotope measurements for tracking water-rock interactions in fractured crystalline rocks at temperatures of up to 43°C. The 17 groundwater samples originate from water-conducting fractures within two specific crystalline rock units, which are characterized by a similar rock mineralogy, but significantly different fluid composition. In particular, the aqueous Li concentrations observed in samples from the two units vary from 1-4 mg/L to 0.01-0.02 mg/L. Whereas δ^7Li values from the unit with high Li concentrations are basically constant (δ^7Li=8.5-9.1‰), prominent variations are

recorded for the samples from the unit with low Li concentrations (δ^7Li=10-41‰). This observation demonstrates that Li isotope fractionation can be highly sensitive to aqueous Li concentrations. Moreover, δ^7Li values from the unit with low Li concentrations correlate well with reaction progress parameters such as pH and [Li]/[Na] ratios, suggesting that δ^7Li values are mainly controlled by the residence time of the fracture groundwater. Consequently, 1D reactive transport modeling was performed to simulate mineral reactions and associated Li isotope fractionation along a water-conducting fracture system using the code TOUGHREACT. Modeling results confirm the residence time hypothesis and demonstrate that the absence of δ^7Li variation at high Li concentrations can be well explained by limitation of the amount of Li that is incorporated into secondary minerals. Modeling results also suggest that Li uptake by kaolinite forms the key process to cause Li isotope fractionation in the investigated alkaline system (pH>9), and that under slow flow conditions (<10 m/year) this process is associated with a very large Li isotope fractionation factor ($\varepsilon \approx -50$ ‰). Moreover, our simulations demonstrate that for simple and well-defined systems with known residence times and low Li concentrations, δ^7Li values may help to quantify mineral reaction rates if more thermodynamic data about the temperature-dependent incorporation of Li in secondary minerals as well as corresponding fractionation factors become available in the future. In conclusion, δ^7L values may be a powerful tool to track water-rock interaction in fractured crystalline rocks at temperature higher than those at the Earth's surface, although their use is restricted to low Li concentrations and well defined flow systems.

1. INTRODUCTION

45 The intensity of water-rock interaction in fractured crystalline rocks forms a key parameter
46 in various applications within the field of environmental geochemistry. Examples include
47 enhanced geothermal systems (EGS) where heat extraction mainly depends on accessible
48 fracture surface areas and where water-rock interaction may cause permeability and porosity to
49 decrease over time (Alt-Epping et al., 2013; Stober and Bucher, 2015), nuclear waste repositories
50 to be constructed in crystalline rock environment (e.g., Nordstrom et al., 1989; Molinero et al.,
51 2008; Gimeno et al., 2014) and groundwater contamination affecting fractured crystalline
52 aquifers. The intensity of water-rock interaction in (fractured) crystalline rocks was also
53 proposed to be essential for the global carbon cycle because the interaction of meteoric water
54 with silicate minerals (i.e., chemical weathering) forms an important CO_2 sink (e.g., Berner et al.,
55 1983; Gislason et al., 1996; Francois and Godderis, 1998).
56 Lithium is a trace element that is almost exclusively found in silicate minerals, which
57 makes it a useful tracer for tracking the interaction between water and silicate minerals such as
58 during chemical silicate weathering (Kisakürek et al., 2005; Pogge von Strandmann et al., 2006;
59 Vigier et al., 2009; Millot et al., 2010b; Liu et al., 2015). In particular, tracking Li isotope
60 fractionation is a powerful tool because the two stable Li isotopes (^{6}Li, ^{7}Li) significantly
61 fractionate during transformation of primary silicate minerals into secondary minerals (Zhang et
62 al., 1998; Pistiner and Henderson, 2003; Vigier et al., 2008; Wimpenny et al., 2010). It is
63 generally agreed that Li isotope fractionation is mainly associated with secondary mineral
64 precipitation whereas Li isotopes dissolve stoichiometrically during (primary) silicate mineral
65 dissolution (Pistiner and Henderson, 2003; Huh et al., 2004). Li isotope fractionation is also
66 promising to track water-rock interaction at temperatures higher than those at the Earth's surface.
67 Vigier et al. (2008) experimentally showed that at a temperature of 250°C the Li isotope

68 enrichment factor for structural Li incorporation into smectite is -1.6‰ and thus greater than the
69 measurement uncertainty for Li isotope measurements. Moreover, Marschall et al. (2007) used a
70 temperature dependent enrichment factor based on a compilation of other studies (Chan et al.,
71 1993; Wunder et al., 2006) to simulate the fate of Li isotopes in subducting slabs suggesting that
72 the Li isotope enrichment factor at 250°C is on the order of -6‰.

73 The numerous studies focusing on chemical silicate weathering at the Earth's surface
74 demonstrate a large range in δ^7Li (2-43‰) of dissolved Li, mostly from river waters (e.g., Huh et
75 al., 1998; Kisakürek et al., 2005; Pogge von Strandmann et al., 2006; Millot et al., 2010b;
76 Dellinger et al., 2015; Liu et al., 2015). Whereas the literature agrees that increasing the ratio of
77 Li uptake by secondary minerals to Li release from primary mineral dissolution drives δ^7Li to
78 higher values, it is still under debate if and how temporal and spatial δ^7Li distributions can be
79 used as a proxy for geomorphic and/or climatic variations. In particular, the increasing seawater
80 δ^7Li values observed over the last ca. 56 Ma (Misra and Froelich, 2012) have been attributed
81 either to increasing tectonic activities (Misra and Froelich, 2012; Li and West, 2014; Wanner et
82 al., 2014) or to a decreasing soil production rate and thus to cooler climatic conditions (Vigier
83 and Goddéris, 2015). In contrast to surface water samples, δ^7Li in water from hydro-geothermal
84 sites with temperatures of up to 335°C varies only in a narrow range of 0-11‰ (Chan et al.,
85 1993; Chan et al., 1994; Millot and Negrel, 2007; Millot et al., 2010a; Henchiri et al., 2014;
86 Sanjuan et al., 2014; Pogge von Strandmann et al., 2016). Despite this relatively narrow range it
87 was proposed that for such systems δ^7Li may operate as a geothermometer to estimate the
88 corresponding reservoir temperature. Also it was proposed to use δ^7Li from hydro-geothermal
89 sites as proxy for the origin of the hydrothermal fluid, and/or as proxy for the intensity of water-
90 rock interaction (Millot and Négrel, 2007; Millot et al., 2010a).

In this study, we present Li isotope measurements of groundwater collected during the construction of the 57 km long Gotthard rail base tunnel in Switzerland. Major anion and cation concentrations have been reported by Seelig and Bucher (2010) and Bucher et al. (2012). Our groundwater samples originate from water-conducting fractures within two specific crystalline rock units and show on-site temperatures of up to 43°C. The hydrogeochemical conditions are thus similar to those at future EGS sites although the temperature is significantly lower than the target EGS temperature of 180°C or greater. The main objective was to explore the use of Li isotope measurements to track water–rock interaction in an EGS-like system with temperatures higher than those at the Earth's surface. Furthermore, an essential part of our study was to simulate Li isotope fractionation occurring in a fractured crystalline aquifer using the reactive transport modeling code TOUGHREACT V3 (Xu et al., 2014). In this context, TOUGHREACT was updated to allow defining a maximum amount of Li that can be incorporated into secondary minerals.

2. SITE DESCRIPTION AND SAMPLING

The new 57 km long Gotthard rail base tunnel in Switzerland is the longest and deepest tunnel in the world. The tunnel crosses the Alps at a base level of ca. 500 m a.s.l. and its construction was divided into five sections, which were excavated separately by drilling vertical access shafts. Our study relates to the Amsteg section in the northern part of the tunnel (Fig 1). This 11.5 km long section was constructed between 2003 and 2006 using a 400 m long tunnel-boring machine (TBM). The section exclusively penetrates crystalline basement rocks of the Aar massif, which is a NE-SW trending complex of Variscan basement overprinted by Alpine metamorphism and deformation (Abrecht, 1994; Schaltegger, 1994; Labhart, 1999). The units

intersected along the Amsteg section show a similar mineralogical composition with dominating quartz, albite, K-feldspar and chlorite and minor amounts of biotite and muscovite as well as secondary calcite and accessory pyrite (Bucher et al., 2012). The thickness of the rock column above the tunnel is up to 2200 m (Fig. 1). According to Bucher et al. (2012) the chemical composition of groundwater samples at tunnel level is dominated by the infiltration of meteoric water at the surface and subsequent reaction with the fractured crystalline rocks during transport to the tunnel level. This infiltration model agrees with steeply dipping rock units (Fig. 1) and the presence of a predominant, nearly vertical fracture system. Preliminary $\delta^{2}H$ and $\delta^{18}O$ measurements indicate a dominating meteoric origin of groundwater collected. More information regarding the geology and hydrology of the Amsteg section is provided by Bucher and al. (2012) and references therein.

A total of 122 groundwater samples were collected from water conducting fractures. Groundwater samples were collected from natural inflows along fractures after these were cut by the TBM and before they were sealed with concrete. Due to the induced pressure drop the water was flowing from the fractures with discharge rates between $3x10^{-4}$ L/s and 6 L/s. Based on differences in dissolved Li concentrations, 17 groundwater samples from two distinct geological units within the Amsteg section, the Bristner Granite and the migmatitic unit called BuMigIII (Fig. 1) were selected for the analyses of Li and Li isotopes. In addition, Li concentrations were determined on rock samples of the two units that were retrieved from cored test drillings performed in front of the TBM. At similar average water influx into the tunnel (Bucher et al., 2012), groundwater draining the Bristner Granite shows Li concentration between 1-4 mg/L and much lower concentrations of 0.01-0.02 mg/L in the BuMigIII.

3. METHODS

3.1. Li concentration measurements

3.1.1. Solid Li

Bulk rock Li concentrations were measured by atomic adsorption spectroscopy using a Vario 6 spectrometer from Analytic Jena at the University of Freiburg, Germany. To do so, cores retrieved from test drillings into the Bristner Granite and into BuMigIII were milled to a fine powder. For each sample 0.1 g was digested in 5 mL 65% HNO_3 and 1 mL 33% H_2O_2. To ensure that the entire sample was digested, samples were exposed to 160°C for 6 minutes and to 215°C for 25 minutes using a MLS microwave. The analytical uncertainty was ±5%.

Selected trace element concentrations including Li of individual mineral phases and phase mixtures within the Bristner Granite and BuMigIII were measured by Laser ablation ICP-MS at the University of Bern, Switzerland, on polished thin sections (50 μm). The system at the University of Bern consists of a Geolas Pro 193 nm ArF Excimer laser (Lambda Physik, Germany) coupled with an ELAN DRCe quadrupole mass spectrometer (QMS; Perkin Elmer, USA). Details on the setup and optimization strategies are given in Pettke et al. (2012). Daily optimization of the analytical conditions were performed to satisfy a ThO production rate of <0.2 % (i.e., Th/ThO intensity ratio < 0.002) and to achieve robust plasma conditions monitored by a Th/U sensitivity ratio of 1 as determined on the SRM610 glass standard. External standardization was performed employing SRM610 from NIST with preferred values reported in Spandler et al. (2011), and bracketing standardization provided a linear drift correction. Internal standardization was done by summing the major element oxides to 100 wt% or 98-97 wt% for biotite and

160 hydrous mineral mixtures (containing muscovite, biotite, minor chlorite and Fe_2O_3). Data were
161 reduced using SILLS (Guillong et al., 2008), with limits of detection calculated for each element
162 in every analysis following the formulation detailed in Pettke et al. (2012).
163
164 *3.1.2. Dissolved Li*
165 Li concentrations available from the previous study (Bucher et al., 2012) were determined
166 using a DX-120 ion chromatograph (IC) with a detection limit of 0.01 mg/L and an analytical
167 uncertainty of 0.005 mg/L for concentrations below 0.1 mg/L. Because groundwater samples
168 originating from BuMigIII displayed Li concentrations on the order of the detection limit (0.01-
169 0.02 mg/L), Li concentration measurements were repeated for these samples using an Analytic
170 Jena ContrAA 700 BU atomic adsorption spectrometer in the graphite furnace mode (GFAAS) at
171 the University of Bern. Standardization was performed using the Merck 4 Certipur standard and
172 tested with the Sigma 6 and Merck 4 Li single element standards. Within the standardization
173 range of 1.25–5 µg/L the Li recovery was >90% yielding an analytical uncertainty of ±10%.
174 Reported Li concentrations are average values of triplicate analyses.
175
176 **3.2. Li isotope measurements**
177 Lithium isotope measurements of groundwater samples were performed as detailed in
178 Pogge von Strandmann and Henderson (2015) and Pogge von Strandmann et al. (2011). Briefly,
179 this entailed running approximately 20 ng of Li through a two-step cation exchange column
180 method, containing AG50W X-12 resin, and using dilute HCl as an eluent.
181 Samples were then analysed on a Nu Instruments HR MC-ICP-MS at Oxford University,
182 by sample-standard bracketing with the standard L-SVEC. Individual analyses consisted of three

separate repeats of 10 ratios (10 s integration time per ratio), giving a total integration time of 300 s/sample during each analytical session. At an uptake rate of 75 µl/min, the sensitivity for a 20 ng/ml solution is ~18 pA of ^{7}Li using 10^{11} Ω resistors. Background instrumental Li intensity, typically ~0.01pA, was subtracted from each measurement. Li isotope measurements are reported as ^{7}Li/^{6}Li ratio in terms of the δ-notation relative to the Li isotope standard L-SVEC (δ^{7}Li =0.0‰) and are given in ‰

$$\delta^{7}Li = \left[\left(\frac{{}^{7}Li/{}^{6}Li_{sample}}{{}^{7}Li/{}^{6}Li_{L-SVEC}} \right) - 1 \right] \cdot 1000 \quad (1)$$

To assess accuracy and precision, both seawater and the international USGS standard BCR-2 were analysed. Both standards analysed with these samples (seawater: δ^{7}Li = 31.5 ± 0.4‰; BCR-2: 2.7 ± 0.3‰) agree well with their long-term averages (seawater: 31.2 ± 0.6‰, n=46; BCR-2: 2.6 ± 0.3‰, n=17; Pogge von Strandmann et al., 2011, Pogge von Strandmann and Henderson, 2015). The total procedural blank for Li isotopes is effectively undetectable (<0.005 ng Li).

3.3. Reactive transport modeling

A series of 1D reactive transport simulations using TOUGHREACT V3 (Xu et al., 2014) was performed to simulate the interaction of infiltrating meteoric water with granitic rock and its specific effects on aqueous δ^{7}Li. TOUGHREACT has been previously applied to evaluate isotopic fractionation coupled to water-rock interaction and hydrological processes in a variety of subsurface environments and laboratory experiments (Sonnenthal et al., 1998; Singleton et al., 2005; Wanner and Sonnenthal, 2013). Specifically, it has been used to simulate Li isotope fractionation in granitic as well as basaltic systems (Wanner et al., 2014; Liu et al., 2015).

Furthermore, the TOUGHREACT approach for simulating isotopic fractionation coupled to mineral precipitation has been recently benchmarked (Wanner et al., 2015).

3.3.1. Model formulation

Mineral dissolution and precipitation

TOUGHREACT V3 (Xu et al., 2014) computes mineral dissolution and precipitation reactions (mol/s/kg_{H2O}) as kinetic reactions based on transition state theory (TST) (Lasaga, 1984)

$$r = A_r \cdot k \cdot \left[1 - \left(\frac{Q}{K}\right)^m\right]^n = A_{rfrac} \cdot k \cdot \left[1 - \left(\frac{Q}{K}\right)^m\right]^n \quad (2)$$

where A_r refers to the mineral reactive surface area (m^2/kg_{H2O}). In case of fracture flow A_r is assumed to be the same for each mineral (Xu et al., 2014) and corresponds to the reactive surface area of the simulated vertical fracture system A_{rfrac}. Q and K refer to the ion activity product and equilibrium constant of a mineral dissolution/precipitation reaction, respectively. Exponents m and n are fitting parameters that must be experimentally determined. However, for or this study they were taken to be unity. The temperature and pH dependent rate constant k is formulated as

$$k = k_{25}^{n}\exp\left[\frac{-E_a^n}{R}\left(\frac{1}{T} - \frac{1}{298.15}\right)\right] + k_{25}^{ac}\exp\left[\frac{-E_a^{ac}}{R}\left(\frac{1}{T} - \frac{1}{298.15}\right)\right]a_{H^+}^{m_{ac}} + k_{25}^{ba}\exp\left[\frac{-E_a^{ba}}{R}\left(\frac{1}{T} - \frac{1}{298.15}\right)\right]a_{H+}^{m_{ba}}$$

(3)

where k_{25} refers to reaction rate constants at 25°C (mol/m^2/s), E_a is the activation energy (kJ/mol) and T and R are the temperature (K) and ideal gas constant, respectively. The superscripts n, ac

227 and *ba* denote neutral, acidic and basic conditions, respectively, a_{H+} refers to the H^+ activity, and
228 m_{ac} and m_{ba} refer to the reaction order with respect to H^+ (i.e., pH) at acidic and basic conditions,
229 respectively. In order to calculate effective precipitation and dissolution rates (eqs. 2,3), reaction
230 rate constants were defined according to the compilation of Palandri and Kharaka (2004)
231 whereas equilibrium constants were taken from the Soltherm.H06 database (Reed and Palandri,
232 2006). Mineral stoichiometries, thermodynamic and kinetic parameters of minerals considered
233 for our simulations are summarized in Table 1.
234
235 *Simulation of Li isotope fractionation*
236 The fate of individual Li isotopes was simulated according to the approach recently
237 presented by Wanner et al. (2014). To do so, ^{6}Li and ^{7}Li were defined as primary aqueous
238 species and were incorporated into the mineral stoichiometry of Li-bearing minerals. Similar to
239 the model of Bouchez et al. (2013) our approach does not distinguish between Li exchange-, Li
240 surface complexation or Li incorporation into a crystal. Accordingly, Li isotope fractionation is
241 solely simulated during Li incorporation of dissolved Li into precipitating minerals. Besides the
242 lack of fractionation factors distinguishing between Li incorporation, Li exchange and sorption
243 the low exchange capacity of crystalline rocks (Mazurek et al., 2003) is supportive to such
244 assumption. Incorporation of Li in secondary clay minerals is limited and occurs only at trace
245 concentrations in the ppm range (e.g., Tardy et al., 1972). The concentration differences by
246 orders of magnitudes between major and trace elements in such secondary minerals may pose
247 convergence problems due to the large differences in exponents in the ion-activity product
248 included in the rate law (eq. 2). To circumvent this problem, precipitation of Li-bearing
249 secondary minerals was simulated defining a solid solution with three different endmembers (see

Wanner et al., 2014): (i) a pure, non Li-bearing secondary mineral endmember, (ii) a pure ^{6}Li endmember and (iii) a pure ^{7}Li endmember. The pure ^{6}Li and ^{7}Li endmembers are hypothetical, but their specification solves the above mentioned numerical problems, and their log(K) values are obtained by fitting to the observed aqueous Li concentration and the amounts of Li analyzed in secondary minerals. The precipitation rate r_{prec} of the solid solution of Li-bearing secondary minerals is then calculated as the sum of the individual endmember precipitation rates r_{2ndmin} (pure secondary mineral), r_{6Li} and r_{7Li}:

$$r_{prec} = r_{2nd\,\min} + r_{^{6}Li} + r_{^{7}Li} \tag{4}$$

The rate of a specific endmember, r_{endm}, is calculated according to a TST-like expression

$$r_{endm} = A \cdot k \cdot \left(1 - \frac{Q_{endm}}{K_{endm}}\right) + k \cdot A \cdot \left(x_{endm} - 1\right) \tag{5}$$

where x_{endm} refers to the mole fraction of a specific secondary mineral endmember. For the hypothetical, pure ^{6}Li and ^{7}Li endmembers x_{6Li} and x_{7Li} are calculated according to:

$$x_{^{6}Li} = \frac{\left(Q_{^{6}Li} / K_{^{6}Li}\right)}{\left(Q_{^{6}Li} / K_{^{6}Li}\right) + \left(Q_{^{7}Li} / K_{^{7}Li}\right) + \left(Q_{2nd\,\min} / K_{2nd\,\min}\right)} \tag{6}$$

$$x_{^{7}Li} = \frac{\left(Q_{^{7}Li} / K_{^{7}Li}\right)}{\left(Q_{^{6}Li} / K_{^{6}Li}\right) + \left(Q_{^{7}Li} / K_{^{7}Li}\right) + \left(Q_{2nd\,\min} / K_{2nd\,\min}\right)} \tag{7}$$

Equations (6) and (7) ensure that the amount of Li that is incorporated into a secondary mineral reflects the Li concentration of the aqueous solution. Accordingly, the amount of Li removed by precipitation increases with increasing aqueous Li concentration. By doing so, our model is in agreement with an experimental study showing that Li concentrations of synthesized smectites are correlated with corresponding aqueous Li concentrations (Decarreau et al., 2012). However, Deccareau et al. (2012) also showed that the total amount of Li that can be incorporated is limited due to structural reasons. We therefore updated TOUGHREACT so that the user now has the option to specify the maximum amount of Li that is allowed to precipitate in a given solid solution. To do so the user needs to define the maximum Li mol fraction $x_{maxLi} = x_{6Li}+x_{7Li}$ that corresponds to a particular maximum Li content (e.g., in μg/g) in a specific mineral solid solution phase. For the pure (hypothetical) ^{6}Li and ^{7}Li endmembers the maximum mol fraction then become

$$x_{^{6}Li\_\max} = x_{\max Li}\frac{\left(Q_{^{6}Li}/K_{^{6}Li}\right)}{\left(Q_{^{6}Li}/K_{^{6}Li}\right)+\left(Q_{^{7}Li}/K_{^{7}Li}\right)} \quad (8)$$

$$x_{^{7}Li\_\max} = x_{\max Li}\frac{\left(Q_{^{7}Li}/K_{^{7}Li}\right)}{\left(Q_{^{6}Li}/K_{^{6}Li}\right)+\left(Q_{^{7}Li}/K_{^{7}Li}\right)} \quad (9)$$

Subsequently, x_{6Li_max} and x_{7Li_max} are compared with x_{6Li} and x_{7Li} as calculated by equations (6) or (7). If $x_{6Li} > x_{6Li\_max}$ and $x_{7Li} > x_{7Li\_max}$ the precipitation rate of the pure ^{6}Li and ^{7}Li endmembers are no longer calculated according to equation (5) and become

$$r_{^{6}Li} = r_{pure2nd}\cdot x_{^{6}Li\_\max} \quad (10)$$

$$r_{^7Li} = r_{pure2nd} \cdot x_{^7Li\_\max} \quad (11)$$

Using the solid solution approach described above allows defining an experimentally determined or otherwise inferred isotope fractionation factor α and corresponding enrichment factor ε associated with mineral precipitation for a particular simulation run:

$$\alpha = \frac{K_{^6Li}}{K_{^7Li}} \quad (12)$$

$$\varepsilon = (\alpha - 1) \cdot 1000 \approx \Delta^7 Li = \delta^7 Li_{2ndMin} - \delta^7 Li_{solution} \quad (13)$$

It should be noted that our approach for simulating Li isotope fractionation is different from other approaches (Lemarchand et al., 2010; Bouchez et al., 2013; Pogge von Strandmann et al., 2014). Instead of exclusively focusing on the Li system, we use a fully-coupled reactive transport modeling code (see Steefel et al., 2015 for a summary of available codes). In doing so, our approach may simulate the chemical evolution of an entire porous media and parameters other than aqueous Li concentrations and δ^7Li values can be used to constrain the model as well.

4. RESULTS

4.1. Solid [Li] measurements

Li concentration data of primary minerals and mineral mixtures from the Bristner Granite and the migmatitic unit BuMigIII are summarized in Table 2. The full chemical analysis of each

313 laser ablation ICP-MS measurement is listed in the electronic appendix. Bulk rock Li
314 concentrations average at 6 for the Bristner Granite and 9 μg/g for BuMigIII. In both units,
315 elevated average Li concentrations of 463 (Bristner Granite) and 217 μg/g (BuMigIII) were
316 observed in sheet silicates such as chloritized biotite and muscovite. Further differences between
317 the two units include higher Li concentrations in K-feldspar (45 μg/g) of the BuMigIII compared
318 to those in K-feldspar (2.4 μg/g) of the Bristner Granite (Table 2).
319
320 **4.2. Aqueous Li concentrations and δ^7Li values**
321 Concentrations and δ^7Li values of aqueous Li of 17 groundwater samples originating from
322 the Bristner Granite and BuMigIII are presented in Table 3 in conjunction with field parameters
323 and major cations and anions concentrations reported in Bucher et al. (2012). Computed
324 saturation indices of selected primary and secondary minerals are listed in Table 4. Groundwater
325 temperature correlates with the thickness of the rock column above the tunnel. In the Bristner
326 Granite groundwater discharges at temperatures from 21.5 to 25.1°C at a corresponding rock
327 overburden of <500 m. In the BuMigIII groundwater temperature is remarkably constant (42.6-
328 43.7°C) at a corresponding overburden of ca. 2000 m, except for sample A103 (36.7°C), which
329 also displays differences in the chemical composition (e.g., Ca, Mg, pH). Groundwater sample
330 A126 displays strongly elevated SO_4 and Ca concentrations compared to the majority of
331 BuMigIII groundwater (Table 3). In accordance with the anhydrite saturation index close to zero
332 (Table 4) this was attributed to anhydrite dissolution during flow along anhydrite-bearing
333 fractures (Bucher et al., 2012). Aqueous Li concentrations vary between 1.6 and 3.2 mg/L in
334 groundwater from the Bristner Granite compared to 0.010 and 0.017 mg/L in groundwater from

335 the BuMigIII. The orders of magnitude difference in Li concentration is striking given the
336 similarity of the bulk rock Li concentrations, which differ only by a factor of about 1.5 (Table 2).
337 Similar to aqueous Li concentrations, δ^7Li values of groundwater from the two units show
338 a distinct behavior. The high-Li groundwater of the Bristner Granite show very little variation in
339 their δ^7Li values (8.5-9.1‰). In contrast, the low-Li groundwater from BuMigIII show a very
340 strong variation (10-41‰). These latter groundwaters display a positive correlation between δ^7Li
341 values and pH but a negative correlation between δ^7Li and aqueous Li concentrations and the
342 molar Li/Na ratio, except for the exceptional groundwater samples A103 and A126 as discussed
343 above (Fig. 2a-c). Moreover, δ^7Li and Li seem to follow a Rayleigh-type fractionation model
344 with α = 0.95 (ε = -50‰) (Fig. 2d), suggesting a single process being responsible for the
345 observed variation in δ^7Li values.
346
347 **5. DISCUSSION**
348
349 **5.1. Source of aqueous Li**
350 Seelig and Bucher (2010) demonstrated that Cl is a passive tracer in groundwater of the
351 Amsteg section of the Gotthard rail base tunnel and suggested that Cl is derived from porewaters
352 trapped in the matrix of the crystalline rocks. Further, they proposed that the trapped porewater
353 represents the remnants of a hydrothermal fluid that evolved during alpine metamorphism.
354 Interestingly, in the Bristner Granite groundwater Li concentrations correlate well with Cl
355 concentrations (r^2=0.95, Fig. 3) inferring that Li is likely derived from the same porewater source
356 as Cl. This observation is important because it demonstrates that meteoric water infiltrating into

357 a crystalline basement may pick up Li from sources other than from interaction with rock
358 forming minerals.

359 In contrast to the Bristner Granite groundwater, Cl and Li concentrations in BuMigIII
360 groundwater are orders of magnitude lower and no clear correlation is observed (Table 3). The
361 molar Cl/Li ratio, however, is of the same order of magnitude as recorded for the Bristner
362 Granite water samples (10-30). This observation suggests that a porewater of a similar
363 composition may form a major Li source for BuMigIII groundwater as well. Alternative Li
364 sources are the dissolution of Li-bearing minerals or mixing of the infiltrating meteoric water
365 with an external groundwater (i.e, originating from another lithology) characterized by an
366 elevated Li concentration and a similar Li/Cl ratio as observed in the Bristner Granite
367 groundwater.

368

369 **5.2. Secondary minerals**

370 Lithium uptake by precipitation of Fe- and Al-bearing secondary mineral or adsorption of
371 Li to these minerals have been proposed to form the major process for Li isotope fractionation
372 observed in the shallow subsurface (Zhang et al., 1998; Pistiner and Henderson, 2003; Vigier et
373 al., 2008; Wimpenny et al., 2010). Based on computed saturation indices (Table 4), kaolinite is
374 the only secondary Al-bearing secondary phase that is potentially precipitating from the
375 BuMigIII groundwater under the given condition (SI>0), whereas the Bristner Granite
376 groundwater is supersaturated with respect to gibbsite and illite as well. To assess the
377 precipitation of kaolinite from BuMigIII groundwater it has to be acknowledged that the
378 equilibrium constant of kaolinite is associated with a large uncertainty (Trotignon et al., 1999),
379 which is reflected by its changing saturation state in BuMigIII groundwater when using different

thermodynamic databases (Table 4). The range of log(K) values for kaolinite tabulated in different thermodynamic databases is at least partly related to differences in solubility experiments (e.g. acid vs alkaline conditions, temperature), but also to analytical difficulties (e.g. Al and Si colloids). Figure 4 shows the relation of the kaolinite equilibrium constant tabulated in the Soltherm.H06 (Reed and Palandri, 2006) and EQ3/6 database (Wolery, 1992). Temperature dependent log(K) tabulated in the Soltherm.H06 database reproduce well log(K) values derived from kaolinite solubility experiments performed at temperatures of 60, 90 and 110°C and at similar pH values as observed in our system (up to pH 9) (Devidal et al., 1996). In contrast, temperature dependent log(K) values derived from the EQ3/6 database (Wolery, 1992) overestimate the Devidal et al. (1996) values. However, they are within the range of kaolinite solubilities determined for temperatures between 22-25°C (Polzer and Hem, 1965; Kittrick, 1966; Reesman and Keller, 1968; May et al., 1986; Yang and Steefel, 2008) and the solubility experiment performed by Nagy et al., (1991) at 80°C and pH 3. Overall, computed saturation indices (Table 4) and thermodynamic considerations (Fig. 4) supports the use of the Soltherm.H06 database and suggests that kaolinite is the dominating secondary Al phase precipitating from the BuMigIII groundwater. The restricted access to water-conducting fractures, however, did not allow confirmation of the presence of kaolinite although it has been observed as low–T alteration product in various crystalline rock environments (e.g., Grimaud et al., 1990; Michard et al., 1996; Gimeno et al., 2014).

Our groundwater samples display dissolved oxygen concentrations below detection limit demonstrating that reducing conditions are established. Under reducing conditions the formation of Fe(III)-oxides such as goethite, ferrihydrite, lepidocrocite, and hematite is absent (Schwertmann, 1988). Accordingly, their formation and corresponding sorption reactions are

403 restricted to the domain very close to the surface where the dissolved oxygen concentration in
404 infiltrating meteoric water is in equilibrium with atmospheric oxygen. The limited formation of
405 Fe-bearing secondary minerals infers that Li isotope fractionation is primarily caused by Li
406 uptake by kaolinite (BuMigIII) or other Al-bearing secondary minerals (Bristner Granite).
407
408 **5.3. Diffusive Li isotope fractionation and anthropogenic Li contamination**
409 If Li influx into the fracture groundwater were occurring entirely by diffusion from a
410 porewater Li source, diffusive fractionation is a likely process to cause a δ^7Li variation in
411 addition to Li uptake by secondary minerals (Richter et al., 2006; Bourg and Sposito, 2007).
412 Owing to the difference in mass the diffusion coefficient of ^{6}Li is larger than that for ^{7}Li leading
413 to enrichment in ^{6}Li (low δ^7Li) in the groundwater. Accordingly, diffusive Li isotope
414 fractionation would partially mask the δ^7Li increase inherited from Li isotope fractionation
415 associated with secondary mineral precipitation. Indeed it would yield an even higher intrinsic
416 fractionation factor than the -50‰ obtained from the Rayleigh-type model (Fig. 2d).
417 In contrast to diffusive Li isotope fractionation, anthropogenic contamination of Li can be
418 excluded based on the infiltration area in remote high-alpine area and the high hydraulic pressure
419 of about 100 bar at the discharge locations (Masset and Loew, 2013). Also, if any artifacts
420 occurred during sampling major species concentrations were affected as well and their
421 concentrations could not be approximated by solely simulating water-rock interaction between
422 meteoric water and pristine granite such as shown below.
423
424 **5.4. Hypothesis for observed δ^7Li variation**

425 The most striking observation from our measurements is that significant δ^7Li variation only
426 occurs at low Li concentrations suggesting that the variation is highly sensitive to the aqueous Li
427 concentration. The second key observation is the negative correlation between δ^7Li and the Li
428 concentration as well as the positive correlation between δ^7Li and pH seen in the BuMigIII
429 groundwater (Fig. 2a,b). Our approach is to first explore the process(es) controlling the Li
430 system in a single hydrogeochemical system such as the BuMigIII groundwater, before
431 comparing the different settings (BuMigIII vs. Bristner Granite).

432 The BuMigIII groundwaters likely have different residence times within the rock column
433 above the tunnel due to a variation in fracture permeability and connectivity. Variable residence
434 times are consistent with the 2 orders of magnitude variation in flow rates (Table 3) and the
435 observed trends in chemical and Li-isotope composition (Fig. 2a,c). In granitic systems, the pH
436 increases with reaction progress (Nordstrom et al., 1989; Grimaud et al., 1990; Bucher et al.,
437 2012; Gimeno et al., 2014) and the Li/Na ratio may form an excellent proxy for the degree of
438 water-rock interaction (e.g., residence time, reaction progress) that inversely correlates with δ^7Li
439 (Liu et al., 2015). The Li/Na ratio is indicative because Na concentrations are several orders of
440 magnitude greater than Li concentrations, and thus not as strongly affected by minor uptake by
441 secondary mineral precipitation (e.g., kaolinite). In case of a discrete Li influx such as from an
442 external groundwater source (Fig. 5b) Na release from primary minerals is ongoing, which also
443 yields a decrease of the Li/Na ratio with flow distance and reaction progress.

444 Higher residence time of groundwater results in increased water-rock interaction and thus
445 increased precipitation of Li-bearing kaolinite, which drives δ^7Li to higher values (Wanner et al.,
446 2014). Observing a negative correlation between δ^7Li and the Li concentration must thus be
447 inherited form the spatial release rate of the actual Li source along the infiltration path in relation

448 to the corresponding Li uptake rate by secondary minerals. The amount of data to quantitatively
449 assess the role of the potential Li sources (Li-bearing minerals, porewater, external
450 groundwater), however, is limited. Therefore and in terms of a sensitivity analyses a series of
451 reactive transport model simulations were performed by varying the Li source as well as the
452 parameters controlling the Li system in order to unravel how these parameters affect aqueous
453 δ^7Li values and Li concentrations in the BuMigIII groundwater.
454
455 **6. REACTIVE TRANSPORT MODELING**
456
457 **6.1. Model setup**
458 Reactive transport model simulations were performed for a simplified vertical, fully-
459 saturated 2000 m long 1D flow path consisting of 1000 grid blocks of 2 m length (Fig. 5). A
460 fixed linear temperature gradient of 10 to 43°C was specified from the upstream to the
461 downstream model boundary. With these specifications, the model represents the geometry
462 where the tunnel intersects with BuMigIII. In contrast to other studies (DePaolo, 2006; Waber et
463 al., 2012; Brown et al., 2013), our model does not explicitly consider diffusion between water
464 flowing along fractures and porewater residing in the intact rock matrix. In doing so, we
465 exclusively simulate reactive transport along one particular fracture system. The porosity and
466 permeability relevant for fluid flow in fractured crystalline rocks depends on the fracture spacing
467 and aperture (Caine and Tomusiak, 2003; MacQuarrie and Mayer, 2005; Sonnenthal et al.,
468 2005). None of these parameters are explicitly known for the present system so that individual
469 simulations were run at a constant flow rate using a fixed fracture porosity of 1% (Fig. 5). To
470 account for the unknown residence time within the rock column above the tunnel simulations

471 were run for flow velocities ranging from 0.2 to 20 m/year, which approximately reflect the
472 variation of flow rates observed for the BuMigIII samples (0.01-2.5 L/s). The specified velocity
473 range also covers the range in hydraulic conductivity (3-7 x 10^{-8} m/s) reported for fracture zones
474 along the nearby Sedrun section of the tunnel (Masset and Loew, 2013).
475
476 **6.2. Initial and boundary conditions**
477 Water in equilibrium with atmospheric CO_2 and O_2 was specified as initial and upper
478 boundary condition to simulate the infiltration of meteoric water into the BuMigIII rock column
479 above the tunnel (Table 5). The solid part of the model domain is given by the granitic
480 composition of the BuMigIII rock (Table 5). Plagioclase has only a minor anorthite component
481 and pure albite was used in the calculations. In contrast, biotite and chlorite were defined as solid
482 solutions between the corresponding Fe (annite and chamosite) and Mg endmembers (phlogopite
483 and clinochlore) according to the analyzed Mg/Fe ratios (el. appendix).
484
485 *6.2.1. Li source and secondary minerals*
486 Li was introduced by defining two different Li sources: (i) Li-bearing biotite with a Li
487 concentration of 217 µg/g as measured in chloritized biotite of the BuMigIII rock (Table 2) and
488 (ii) a hypothetical $Li_{0.04}Na_{0.96}Cl$ solid phase that acts either as a proxy for matrix porewater or an
489 external, ad-mixed groundwater Li source. The Cl/Li ratio of 25 defined for this hypothetical
490 phase corresponds to the ratio obtained from the linear correlation between Cl and Li observed
491 for Bristner Granite groundwater (Fig. 3), while charge balance was maintained by including Na.
492 An initial δ^7Li value of 1.7‰ was assigned to Li-bearing biotite, corresponding to the average
493 δ^7Li value determined for a large series of different granites (Teng et al., 2009). In contrast, the

494 average Bristner Granite groundwater δ^7Li value of 8.7‰ was assigned to the hypothetical
495 $Li_{0.04}Na_{0.96}Cl$ solid phase (Table 3) based on our concept that Li in the BuMigIII is derived from
496 a similar source as in the Bristner Granite.

497 While all simulations considered the Li-bearing biotite source, two scenarios were run for
498 the $Li_{0.04}Na_{0.96}Cl$ source. The first scenario considered a constant zero order dissolution rate of
499 $2x10^{-15}$ mol/kg_{H2O}/s occurring along the entire model domain and corresponding to a Li influx
500 from a porewater source (continuous Li influx scenario, Fig. 5a). This yields a Li concentration
501 of 0.017 mg/L at the tunnel level what corresponds to the maximum concentration observed in
502 BuMigIII groundwater samples (Fig. 2). The second set considered a single point Li influx after
503 an arbitrary flow distance of 400 m and simulates a situation where Li in the BuMigIII
504 groundwater is ad-mixed by an external fracture groundwater to the infiltrating meteoric water
505 (mixing scenario, Fig. 5b). To do so, the Li concentration of the simulated groundwater mixture
506 was set to 0.017 mg/L at z = -400m.

507 Kaolinite is the only secondary Al-phase precipitating in our model and Li uptake by
508 kaolinite is the only process to cause Li isotope fractionation. Based on the observation that the
509 SiO_2 concentrations of the 122 tunnel waters are solubility-controlled by quartz above a pH of
510 ca. 9 (Bucher et al., 2012), secondary quartz was allowed to precipitate as well. The same applies
511 for goethite.

512

513 *6.2.2. Sensitivity analyses*

514 Our approach for simulating Li isotope fractionation allows defining a Li isotope
515 fractionation factor as well as a maximum amount of Li that can be incorporated in secondary
516 minerals. Since both parameters are unknown simulations were run for Li isotope enrichment

517 factors of -25, -37.5 and -50‰ associated with Li uptake by kaolinite and for maximum Li
518 concentrations in kaolinite of 25, 50 and 75 µg/g to test their impact on the model results.
519 Whereas these maximum Li concentrations cover the Li concentration range observed in natural
520 kaolinite (Tardy et al., 1972; Vigier and Goddéris, 2015), Li isotope enrichment factors of -37.5
521 and -50‰ are outside the range inferred so far for secondary mineral precipitation (≈ -10 to -
522 30‰) (Zhang et al., 1998; Huh et al., 2001; Pistiner and Henderson, 2003; Kisakürek et al.,
523 2005; Pogge von Strandmann et al., 2006; Vigier et al., 2008; Pogge von Strandmann et al.,
524 2010). The range in ε was expanded to higher values because the Li concentration and isotope
525 data from BuMigIII groundwater revealed an ε-value of -50‰ when applying a Rayleigh-type
526 model (Fig. 2d). A temperature effect on epsilon such as observed for hydro-geothermal system
527 (Marschall et al., 2007; Vigier et al., 2008; Verney-Carron et al., 2015; Pogge von Strandmann et
528 al., 2016) was not considered because within the temperature range of our model (10-43°C) it is
529 likely smaller than the uncertainty of ε-values reported for Li uptake by secondary minerals as
530 well as the ε-range considered in the sensitivity analyses. Additional sensitivity simulations
531 included a reduction of the kaolinite precipitation rate constant by 67% and 33% of the initially
532 chosen value (base case, Table 1), a variation of the δ^7Li value specified for the $Li_{0.04}Na_{0.96}Cl$
533 phase and a variation of the location of the input of the external groundwater Li source. An
534 overview of the simulated parameter combinations is given in Table 6.
535
536 **6.3. Model results and discussion**
537
538 *6.3.1. General system behavior*

539 The general water-rock interaction progress along the 2000 m model domain is shown for a
540 general situation where the system is reactive enough to approach chemical equilibrium within
541 the model domain (Fig. 6). The profiles shown in Figure 6 are referred to such a general reaction
542 progress because it depends on the product of two unknown parameters such as reactive fracture
543 surface area (A_{rfrac}) and residence time (eq. (2)). If the system was more or less reactive (e.g.,
544 slower flow velocity, higher A_{rfrac}) the profiles except the temperature profile would be
545 horizontaly shifted towards lower or greater distances, respectively, whereas the general profile
546 shape would remain similar.

547 The relative change in mineral volume fraction demonstrates (Fig. 6c) that albite
548 dissolution and kaolinite precipitation are driving the general chemical system in addition to
549 quartz and calcite precipitation, as previously described for low-T crystalline groundwater
550 environments (Nordstrom et al., 1989; Grimaud et al., 1990; Trotignon et al., 1999; Gimeno et
551 al., 2014) and as reflected by the calculated mineral states (Table 4). In contrast, other primary
552 minerals (K-feldspar, chlorite, biotite, muscovite) show only minor volume changes whereas
553 goethite formation is restricted to the first grid block where pyrite is oxidized by oxygen
554 dissolved in the infiltrating meteoric water (Fig. 5). A prominent feature typical for the evolution
555 of crystalline groundwaters is the strong increase in pH from about 8.5 to 9.7, which at the
556 considered reaction progress occurs between 1000 to 1500 m along the model domain (Fig. 6a).
557 The increase in pH is correlated to the maximum albite dissolution and kaolinite formation (Fig.
558 6c). Across this interval, coupled albite dissolution and kaolinite precipitation is thus the main
559 reaction governing the pH increase

560

561 $$NaAlSi_3O_8 + H^+ + 0.5H_2O = 0.5Al_2Si_2O_5(OH)_4 + Na^+ + 2SiO_2 \quad (14)$$

562

563 The actual driving force for reaction (14) is the supply of protons by the dissolution and
564 dissociation of atmospheric CO_2

565

566 $$CO_{2(g)} + H_2O = H_2CO_3 = H^+ + HCO_3^- \quad (15)$$

567

568 Prior to the strong pH increase the system is controlled by calcite, i.e, by the initial
569 dissolution and subsequent precipitation caused by the calcite solubility decrease with increasing
570 temperature ($Ca^{2+}_{(aq)} + HCO_3^-{}_{(aq)} = CaCO_{3(s)} + H^+$) (Fig. 6c). As the Ca^{2+} and HCO_3^-
571 concentrations decrease due to continuous calcite precipitation along the flow path, calcite
572 precipitation is diminished (Fig. 6b,c) and the pH is no longer controlled by calcite precipitation.
573 At this point coupled albite dissolution and kaolinite precipitation is accelerated by the pH
574 dependence of the corresponding rates (*cf.* eq (3), Table 1) as well as by the linear temperature
575 increase along the flow path (Fig. 6a). As the system approaches equilibrium with respect to
576 albite (Fig. 6d), further albite dissolution and subsequent kaolinite precipitation is slowed down
577 and the pH becomes controlled by the speciation of dissolved Si ($H_4SiO_4 = H_3SiO_4^- + H^+$), which
578 becomes important above pH 9-9.5.

579 The maximum in coupled albite dissolution and kaolinite precipitation is reflected by the
580 Na concentration profile showing a maximum increase along the same interval as the strong pH
581 increase (Fig. 6b). In contrast, dissolved Si is controlled by the solubility of quartz, which
582 strongly increases above pH 9 when $H_3SiO_4^-$ becomes the dominant Si species. Owing to the
583 linear temperature increase (Fig. 6a) Na^+, Al^{3+} and Si concentrations are still increasing at the
584 downstream model boundary (Fig. 6b) because the solubility of albite and quartz are increasing

585 with temperature (Table 1). In turn, the pH slightly drops towards the model boundary because
586 of the temperature-dependence of the equilibrium pH.
587
588 *Behavior of Li*
589 The modeled Li concentration of ~0.6 µg/L inherited from biotite dissolution at the tunnel
590 level is very low (not shown) and demonstrates that only minor amounts of aqueous Li can be
591 derived from interaction between the infiltrating meteoric water and the BuMigIII rocks. Such a
592 minor Li contribution is consistent with a molar Mg/Li ratio in the BuMigIII water samples (<14,
593 Table 3) that is much lower than that in chloritized biotite forming the primary Li host of the
594 BuMigIII rock (ca. 65-85, Table 2). An additional Li input such as from the matrix porewater, an
595 external groundwater or an unknown mineral source is thus required to explain the observed Li
596 concentrations (Table 3).
597 For both Li influx scenarios modeled with the hypothetical $Li_{0.04}Na_{0.96}Cl$ phase (Fig. 5),
598 the model yields a strong δ^7Li increase between 1000-1500 m (Fig. 7a,b). At the considered
599 reaction progress this interval corresponds to the maximum in kaolinite precipitation (Fig. 6c).
600 This suggests that Li isotope fractionation is coupled to kaolinite precipitation and that δ^7Li
601 values are highly sensitive to the amount of kaolinite precipitation. Consequently, when kaolinite
602 precipitation slows down towards the downstream model boundary, the δ^7Li increase slows
603 down as well (Fig. 7b) or even starts to decrease (Fig. 7a) depending on the simulated scenario.
604 For the continuous Li influx scenario (Fig. 5a) the Li concentration increases over most
605 part of the domain because the Li influx outpaces the Li uptake by secondary kaolinite
606 precipitation except for a short interval where kaolinite precipitation is maximal (Fig. 7a).
607 Consequently for this scenario δ^7Li is positively correlated to the Li concentration with the

608 exception of the downstream model boundary where δ^7Li is decreasing (Fig. 7a,c) because the Li
609 load in the fracture fluid becomes dominated by the ongoing Li influx with a δ^7Li of 8.7‰. For
610 the mixing scenario (Fig. 5b) the Li concentration decreases after the single point Li input
611 yielding throughout a negative correlation with δ^7Li (Fig. 7b,c).
612
613 *6.3.2. Application to BuMigIII groundwater*
614 The observation that only the mixing scenario yields a negative correlation between δ^7Li
615 and the Li concentration as observed in BuMigIII groundwater (Fig. 2) suggests that Li is
616 inherited from a discrete rather than from a continuous Li influx. Whereas mixing with an
617 external groundwater is a likely candidate for single point Li influx, it is also possible that it
618 occurred from a not yet identified rock type enriched in Li-bearing mineral(s), with a
619 composition that is significantly different from that of the BuMigIII rock exposed at the tunnel
620 level.
621 To further apply the mixing scenario (Fig. 5b) to the BuMigIII system the model was run
622 for a variable reaction progress along the 2000 m long flow path by varying the flow velocity
623 while keeping the reactive fracture surface area constant. Consequently, steady state major
624 species concentrations computed for the tunnel level (z = -2000 m) are plotted against the pH to
625 illustrate their dependence on the overall reaction progress and to compare them with measured
626 BuMigIII groundwater data (Fig. 8). Although the fits are not perfect, the fact that the order of
627 magnitude is reproducible suggests that the model captures the governing mineral reactions.
628 Differences between modeled and observed concentrations are likely inherited from the
629 assumptions of constant flow velocity and homogeneous mineralogy along the flow path.
630

Li system

The sensitivity of our model parameters on the Li system was tested by comparing measured δ^7Li and Li concentrations with computed steady state values obtained at the tunnel level for a variable reaction progress along the flow path and for 7 combinations of Li isotope enrichment factors, maximum Li concentrations in kaolinite, and kaolinite precipitation rate constants. Figure 9 illustrates that all varied parameters have an effect on the Li concentration and/or on δ^7Li. Higher amounts of Li incorporation into kaolinite as well as higher amounts of kaolinite precipitation increase the δ^7Li value and decrease the Li concentration for a given reaction progress (i.e., pH) because both parameters increase the ratio between the Li uptake by kaolinite and the external Li input. Increasing the Li isotope enrichment factor also yields an increase in the δ^7Li value for a given reaction progress (i.e., pH), but does obviously not change the Li concentration. The sensitivity analyses carried out for the location of the single point Li influx yielded only minor dependence as long as it occurred before the system evolved to the maximum kaolinite formation rate (not shown).

In general, simulations performed for the mixing scenario approximate the observed pH dependence of measured δ^7Li values (Fig. 9), although in a non-linear manner, and the observed Li concentrations can be reproduced. The best match between modeled and measured data is obtained for a Li isotope enrichment factor of -50‰, a maximum Li concentration in kaolinite of 75 μg/g and a slightly reduced kaolinite precipitation rate constant (i.e., simulation M7; Fig. 9). A similar fit is obtained, however, when setting the δ^7Li value of the single point Li source to 1.7 ‰ while limiting the amount of Li in kaolinite to 50 μg/g (Fig. 10). The observation that different parameter combinations result in similar good fits demonstrates that the system is under-determined and that not all parameters affecting the Li system can be calibrated in a

654 quantitative way. However, the observed negative correlation between δ^7Li and Li concentration
655 can only be approximated if the Li isotope enrichment factor is as high as -50‰ (Fig. 9). An
656 enrichment factor of -50‰ also corresponds to that obtained from the Rayleigh-type model (Fig.
657 2d). This is an interesting observation because ε=-50‰ is clearly outside the range of Li isotope
658 enrichment factor reported or inferred for secondary mineral precipitation (≈ -10 to -30‰)
659 (Zhang et al., 1998; Huh et al., 2001; Pistiner and Henderson, 2003; Kisakürek et al., 2005;
660 Pogge von Strandmann et al., 2006; Vigier et al., 2008; Pogge von Strandmann et al., 2010),
661 although vigorous determination of the temperature-dependence of Li isotope fractionation
662 involving mineral precipitation have so far only been reported for Li incorporation during
663 smectite precipitation (Vigier et al., 2008). Since a contribution from diffusive Li isotope
664 fractionation would yield an even higher intrinsic enrichment factor and an anthropogenic Li
665 contamination is unlikely, the reason for the high apparent Li isotope enrichment factor is
666 unclear and further research is required to unravel whether this is related to the slow flow rates
667 and/or alkaline conditions of our system.

668 Overall, our model results reveal that the large δ^7Li variation observed in BuMigIII
669 groundwater samples (10-41‰) are related to their pH range of 9.3 to 9.8. Over this pH window
670 the amount of coupled albite dissolution and kaolinite precipitation is at its maximum (Fig. 6).
671 Consequently, a variation in reaction progress along the infiltration path (e.g., variable residence
672 time) strongly affects the amount of Li-bearing kaolinite precipitation and thus the δ^7Li value.
673 Simulation results also reveal that the observed Li isotope fractionation is independent of the
674 origin of Li (ad-mixing of external groundwater, in-diffusion from porewater, dissolution of
675 unidentified minerals) as long as this addition occurred before the infiltrating meteoric water
676 evolved to its maximum kaolinite formation. This latter point further argues against a continuous

677 addition of Li by diffusion from the porewater as there is no reason why such addition should
678 stop at a certain point along the flowpath in the same rock unit.
679
680 *6.3.3. Application to Bristner Granite groundwater*
681 Based on the finding that the mixing scenario (Fig. 5b) can explain the δ^7Li variation
682 observed in BuMigIII samples (Table 3), the same modeling approach was used to explore the
683 sensitivity of δ^7Li on the Li concentration and to particularly test whether the absence of δ^7Li
684 variation in Bristner Granite groundwater is simply caused by its high Li concentration (Table 3).
685 To do so, the mixing scenario (Fig. 5b) was run by setting the Li concentration of the simulated
686 groundwater mixture to 0.017, 0.08, 0.17, and 1.7 mg/L, whereas the other parameters were kept
687 constant at the values used in simulation M7 (Table 6). As can be seen from Figure 11, the
688 simulated δ^7Li values strongly depend on the Li concentration in the groundwater. At a Li
689 concentration representing the range of Bristner Granite groundwater (1.7 mg/L), the predicted
690 δ^7Li value does not differ from the value specified for the single point Li influx (δ^7Li=8.7‰). A
691 change in the δ^7Li values is only obtained if the Li concentration in the groundwater is lowered
692 by a factor of 10 or more. The reason for these effects lies in the amount of Li that was allowed
693 to be incorporated into precipitating kaolinite (75 μg/g). Accordingly, the ratio between Li that is
694 incorporated into kaolinite and Li obtained from the single point influx decreases with increasing
695 Li concentration in such influx. Because this ratio is also reflected in the δ^7Li value, the
696 computed δ^7Li values become lower as the concentration of Li from the influx increases. The
697 ability of the model to predict the absence of δ^7Li at high Li concentration supports the existence
698 of a maximum amount of Li that can be structurally incorporated into precipitating kaolinite,
699 which is in agreement with mineralogical and experimental findings (Tardy et al., 1972;

Decarreau et al., 2012; Vigier and Goddéris, 2015). Such limitation further constitutes the likely reason for the low δ^7Li values and absence of δ^7Li variation observed for the Bristner Granite groundwater where the Li concentration is up to 500 times higher than in BuMigIII groundwater (Table 3).

7. IMPLICATIONS FOR USING δ^7Li AS A WATER-ROCK INTERACTION PROXY

The comparison between analytical and simulation results confirms that for a relatively simple hydrological system aqueous δ^7Li is controlled by the cumulative amount of Li-bearing secondary mineral formation in relation to the Li release from primary mineral or other Li sources (Wanner et al., 2014; Pogge von Strandmann et al., 2016). Because secondary mineral formation is coupled to the dissolution of primary minerals, δ^7Li may be used in conjunction with major species concentrations to estimate mineral reaction rates using modeling approaches such as the one presented here. However, even for mono-lithological systems an accurate quantification of these rates based on δ^7Li remains challenging. The first issue is that δ^7Li values are strongly affected by the reactivity of system (Fig. 9), which is controlled by the flow velocity (or the residence time, respectively), and the reactive surface areas. Secondly, dissolution and precipitation rates of silicate minerals are highly pH and temperature dependent (Fig. 6), demonstrating that the spatial temperature and pH distribution must be known to constrain reaction rates for a given flow system. Finally, our sensitivity analyses suggest that aqueous δ^7Li values are controlled by the amount of Li that can be taken up by secondary minerals, as well as the corresponding fractionation factor (Fig. 9). None of these parameters are fully characterized for the entire suite of Li bearing secondary minerals. For well-constrained hydrogeological systems, however, the listed challenges are likely resolved in the future once more experimental

723 data will become available. Our model results based on actual data from a crystalline
724 groundwater environment at elevated temperatures and including kaolinite precipitation indicate
725 that δ^7Li values might be especially useful to better constrain the formation rate of secondary
726 minerals for which kinetic data is still scarce (Yang and Steefel, 2008 and references therein).
727 Moreover, the strong δ^7Li variation observed at temperatures above those at the Earth's surface
728 (Table 3) demonstrates the potential for using δ^7Li as water-rock interaction proxy at elevated
729 temperatures. If the sensitivity of δ^7Li on the Li concentration, however, is as high as inferred
730 from Figure 11 the use of δ^7Li to constrain mineral reaction rates is restricted to systems with
731 low Li concentrations, which does usually not apply for hydro-geothermal systems (Chan et al.,
732 1994; Millot and Négrel, 2007; Millot et al., 2010a; Sanjuan et al., 2014; Sanjuan et al., 2016).
733 In contrast to well-defined systems, we suspect that quantifying continental silicate
734 weathering rates through time based on sedimentary archives such as the inferred Cenozoic
735 seawater δ^7Li record (Misra and Froelich, 2012) will remain challenging. Due to the strong
736 sensitivity of δ^7Li on the subsurface residence time an accurate quantification requires the
737 quantification of changes in the average subsurface residence time through time (e.g., discharge
738 variations) under a changing climate and at an increasing tectonic activity (Misra and Froelich,
739 2012; Vigier and Goddéris, 2015). Another major challenge is that δ^7Li variations are likely
740 controlled by the corresponding Li concentration such as inferred by our simulation results (Figs.
741 11) and likely manifested by the absence of δ^7Li value observed in the Bristner Granite
742 groundwater. If the sensitivity of δ^7Li on the Li concentration was as high as inferred from our
743 study, the continental Li flux through time needs to be quantified accurately in addition to
744 corresponding discharge variations. First Cenozoic Li flux reconstructions have been already
745 provided by Vigier and Goddéris (2015) and Li and West (2014).

746

747 **8. SUMMARY AND CONCLUSIONS**

748 The use of Li isotope measurements for tracking water-rock interaction in fractured
749 crystalline aquifers at temperatures of up to 43°C was assessed by performing Li isotope
750 measurements on 17 groundwater samples collected during drilling of the new Gotthard rail base
751 tunnel in Switzerland. A particular effort was made to match δ^7Li values as well as major species
752 concentrations by reactive transport model simulations using the code TOUGHREACT V3. In
753 doing so, the possibility of defining a maximum amount of a trace element that is incorporated
754 into the structure of a precipitating mineral was added as a new capability to TOUGHREACT
755 V3. The main conclusions from this study are:

756 1. The alteration of fracture surfaces by a circulating fluid may lead to a strong variation of
757 δ^7Li values at temperatures of up to 43°C. A strong δ^7Li variation, however, was only
758 observed if the Li concentration was low (0.01-0.02 mg/L). For high Li concentrations on
759 the order of 1-4 mg/L no variation was observed suggesting that the amount of Li that can
760 be incorporated into secondary minerals is limited and that the use of δ^7Li values as a
761 proxy for water-rock interaction is restricted to low Li concentrations.
762 2. Li uptake by kaolinite precipitation or by the precipitation of other Al–bearing phases
763 forms the key process to cause Li isotope fractionation in fractured crystalline aquifers
764 characterized by a granitic mineralogical composition. Our data suggests that under slow
765 flow conditions (<10 m/year), at temperatures <50 °C, and alkaline conditions (pH>9),
766 this Li uptake is associated with a very large Li isotope fractionation factor ($\varepsilon \approx$ -50 ‰).
767 3. For the samples with low Li concentrations, δ^7Li values are mainly controlled by the
768 cumulative amount of kaolinite precipitation occurring along the flow path.

Consequently, aqueous δ^7Li values are sensitive to fluid residence times, reactive fracture surface areas, and pH values, all controlling overall silicate mineral reaction rates.

4. Incorporating the fate of Li isotopes into fully coupled reactive transport model simulations allows a predictive understanding of measured Li isotope ratios. For simple and well-defined systems with known residence times and low Li concentrations, δ^7Li values may help to quantify mineral reaction rates and associated parameters (e.g., reactive surface area). An accurate quantification, however, currently suffers from the lack of thermodynamic data such as the temperature dependent amount of Li that can be incorporated into secondary minerals as well as corresponding fractionation factors.
5. In crystalline aquifers with high Li concentrations such as in the Bristner Granite groundwater Li is likely inherited from an ancient hydrothermal fluid still residing in the pore space of the intact rock matrix.

ACKNOWLEDGMENTS

This work is dedicated to H.-J. (Jöggu) Ziegler, head geologist of the Gotthard rail base tunnel who brought CW first into contact with the intriguing water samples from the Gotthard rail base tunnel and who passed away on the same day CW started to look for available samples. CW was supported by the Swiss Competence Center for Energy Research-Supply of Electricity (SCCER-SOE). PPvS and Li isotope analyses were funded by NERC Advanced Research Fellowship NE/I020571/2.

REFERENCES

Abrecht J. (1994) Geologic units of the Aarmassif and their pre-Alpine rock associations: a critical review. *Schweizerische Mineralogische und Petrographische Mitteilungen* **74**, 5-27.

Alt-Epping P., Diamond L. W., Häring M. O., Ladner F. and Meier D. B. (2013) Prediction of water–rock interaction and porosity evolution in a granitoid-hosted enhanced geothermal system, using constraints from the 5 km Basel-1 well. *Appl. Geochem.* **38**, 121-133.

Berner R. A., Lasaga A. C. and Garrels R. M. (1983) The carbonate-silicate geochemical cycle and its effect on atmospheric carbon-dioxide over the past 100 million years. *Am. J. Sci.* **283**, 641-683.

Bouchez J., Von Blanckenburg F. and Schuessler J. A. (2013) Modeling novel stable isotope ratios in the weathering zone. *Am. J. Sci.* **313**, 267-308.

Bourg I. C. and Sposito G. (2007) Molecular dynamics simulations of kinetic isotope fractionation during the diffusion of ionic species in liquid water. *Geochim. Cosmochim. Acta* **71**, 5583-5589.

Brown S. T., Kennedy B. M., DePaolo D. J., Hurwitz S. and Evans W. C. (2013) Ca, Sr, O and D isotope approach to defining the chemical evolution of hydrothermal fluids: Example from Long Valley, CA, USA. *Geochim. Cosmochim. Acta* **122**, 209-225.

Bucher K., Stober I. and Seelig U. (2012) Water deep inside the mountains: Unique water samples from the Gotthard rail base tunnel, Switzerland. *Chem. Geol.* **334**, 240-253.

Caine J. S. and Tomusiak S. R. A. (2003) Brittle structures and their role in controlling porosity and permeability in a complex Precambrian crystalline-rock aquifer system in the Colorado Rocky Mountain front range. *Geological Society of America Bulletin* **115**, 1410-1424.

Chan L.-H., Edmond J. M. and Thompson G. (1993) A lithium isotope study of hot springs and metabasalts from Mid-Ocean Ridge Hydrothermal Systems. *Journal of Geophysical Research: Solid Earth* **98**, 9653-9659.

Chan L.-H., Gieskes J. M., Chen-Feng Y. and Edmond J. M. (1994) Lithium isotope geochemistry of sediments and hydrothermal fluids of the Guaymas Basin, Gulf of California. *Geochim. Cosmochim. Acta* **58**, 4443-4454.

Decarreau A., Vigier N., Pálková H., Petit S., Vieillard P. and Fontaine C. (2012) Partitioning of lithium between smectite and solution: An experimental approach. *Geochim. Cosmochim. Acta* **85**, 314-325.

Dellinger M., Gaillardet J., Bouchez J., Calmels D., Louvat P., Dosseto A., Gorge C., Alanoca L. and Maurice L. (2015) Riverine Li isotope fractionation in the Amazon River basin controlled by the weathering regimes. *Geochim. Cosmochim. Acta* **164**, 71-93.

DePaolo D. J. (2006) Isotopic effects in fracture-dominated reactive fluid–rock systems. *Geochim. Cosmochim. Acta* **70**, 1077-1096.

Devidal J.-L., Dandurand J.-L. and Gout R. (1996) Gibbs free energy of formation of kaolinite from solubility measurement in basic solution between 60 and 170 °C. *Geochim. Cosmochim. Acta* **60**, 553-564.

Francois L. M. and Godderis Y. (1998) Isotopic constraints on the Cenozoic evolution of the carbon cycle. *Chem. Geol.* **145**, 177-212.

Gimeno M. J., Auqué L. F., Acero P. and Gómez J. B. (2014) Hydrogeochemical characterisation and modelling of groundwaters in a potential geological repository for spent nuclear fuel in crystalline rocks (Laxemar, Sweden). *Appl. Geochem.* **45**, 50-71.

Gislason S. R., Arnorsson S. and Armannsson H. (1996) Chemical weathering of basalt in Southwest Iceland; effects of runoff, age of rocks and vegetative/glacial cover. *Am. J. Sci.* **296**, 837-907.

Grimaud D., Beaucaire C. and Michard G. (1990) Modelling of the evolution of ground waters in a granite system at low temperature: the Stripa ground waters, Sweden. *Appl. Geochem.* **5**, 515-525.

Guillong M., Meier D. L., Allan M. M., Heinrich C. A. and Yardley B. W. D. (2008) SILLS: A MATLAB-based program for the reduction of laser ablation ICP-MS data of homogeneous materials and inclusions, in: Sylvester, P. (Ed.), Laser ablation ICP-MS in the Earth Sciences: current practices and outstanding issues, pp. 328-333.

Henchiri S., Clergue C., Dellinger M., Gaillardet J., Louvat P. and Bouchez J. (2014) The Influence of Hydrothermal Activity on the Li Isotopic Signature of Rivers Draining Volcanic Areas. *Proc. Earth Planet. Sci.* **10**, 223-230.

Huh Y., Chan L. H., Zhang L. and Edmond J. M. (1998) Lithium and its isotopes in major world rivers: Implications for weathering and the oceanic budget. *Geochim. Cosmochim. Acta* **62**, 2039-2051.

Huh Y., Chan L. H. and Edmond J. M. (2001) Lithium isotopes as a probe of weathering processes: Orinoco River. *Earth Planet. Sci. Lett.* **194**, 189-199.

Huh Y., Chan L. H. and Chadwick O. A. (2004) Behavior of lithium and its isotopes during weathering of Hawaiian basalt. *Geochem. Geophy. Geosy.* **5**.

Kisakürek B., James R. H. and Harris N. B. W. (2005) Li and δ7Li in Himalayan rivers: Proxies for silicate weathering? *Earth Planet. Sci. Lett.* **237**, 387-401.

Kittrick J. A. (1966) Free energy of formation of kaolinite from solubility measurements. *American Mineralogist* **51**, 1457-&.

Labhart T. P. (1999) Aarmassiv, Gotthardmassiv und Tavetscher Zwischenmassiv: Aufbau und Entstehungsgeschichte, in: Loew, S., Wyss, R. (Eds.), Symposium Geologie Alptransit, Zürich. Balkema, Rotterdam, pp. 31-43.

Lasaga A. C. (1984) Chemical kinetics of water-rock interactions. *J. Geoph. Res.* **89**, 4009-4025.

Lemarchand E., Chabaux F., Vigier N., Millot R. and Pierret M.-C. (2010) Lithium isotope systematics in a forested granitic catchment (Strengbach, Vosges Mountains, France). *Geochim. Cosmochim. Acta* **74**, 4612-4628.

Li G. and West A. J. (2014) Evolution of Cenozoic seawater lithium isotopes: Coupling of global denudation regime and shifting seawater sinks. *Earth Planet. Sci. Lett.* **401**, 284-293.

Liu X.-M., Wanner C., Rudnick R. L. and McDonough W. F. (2015) Processes controlling δ7Li in rivers illuminated by study of streams and groundwaters draining basalts. *Earth Planet. Sci. Lett.* **409**, 212-224.

MacQuarrie K. T. B. and Mayer K. U. (2005) Reactive transport modeling in fractured rock: A state-of-the-science review. *Earth-Sci. Rev.* **72**, 189-227.

Marschall H. R., Pogge von Strandmann P. A. E., Seitz H.-M., Elliott T. and Niu Y. (2007) The lithium isotopic composition of orogenic eclogites and deep subducted slabs. *Earth Planet. Sci. Lett.* **262**, 563-580.

Masset O. and Loew S. (2013) Quantitative hydraulic analysis of pre-drillings and inflows to the Gotthard Base Tunnel (Sedrun Lot, Switzerland). *Eng. Geol.* **164**, 50-66.

May H. M., Klnniburgh D. G., Helmke P. A. and Jackson M. L. (1986) Aqueous dissolution, solubilities and thermodynamic stabilities of common aluminosilicate clay minerals: Kaolinite and smectites. *Geochim. Cosmochim. Acta* **50**, 1667-1677.

881 Mazurek M., Jakob A. and Bossart P. (2003) Solute transport in crystalline rocks at Äspö — I:
882 Geological basis and model calibration. *J. Contam. Hydrol.* **61**, 157-174.
883 Michard G., Pearson Jr F. J. and Gautschi A. (1996) Chemical evolution of waters during long
884 term interaction with granitic rocks in northern Switzerland. *Appl. Geochem.* **11**, 757-774.
885 Millot R. and Negrel P. (2007) Multi-isotopic tracing (delta(7)Li, delta(11)B, (87)Sr/(86)Sr) and
886 chemical geothermometry: evidence from hydro-geothermal systems in France. *Chem.*
887 *Geol.* **244**, 664-678.
888 Millot R. and Négrel P. (2007) Multi-isotopic tracing (δ7Li, δ11B, 87Sr/86Sr) and chemical
889 geothermometry: evidence from hydro-geothermal systems in France. *Chem. Geol.* **244**,
890 664-678.
891 Millot R., Scaillet B. and Sanjuan B. (2010a) Lithium isotopes in island arc geothermal systems:
892 Guadeloupe, Martinique (French West Indies) and experimental approach. *Geochim.*
893 *Cosmochim. Acta* **74**, 1852-1871.
894 Millot R., Vigier N. and Gaillardet J. (2010b) Behaviour of lithium and its isotopes during
895 weathering in the Mackenzie Basin, Canada. *Geochim. Cosmochim. Acta* **74**, 3897-3912.
896 Misra S. and Froelich P. N. (2012) Lithium isotope history of Cenozoic seawater: changes in
897 silicate weathering and reverse weathering. *Science* **335**, 818-823.
898 Molinero J., Raposo J. R., Galíndez J. M., Arcos D. and Guimerá J. (2008) Coupled
899 hydrogeological and reactive transport modelling of the Simpevarp area (Sweden). *Appl.*
900 *Geochem.* **23**, 1957-1981.
901 Nagy K. L., Blum A. E. and Lasaga A. C. (1991) Dissolution and precipitation kinetics of
902 kaolinite at 80 degrees C and pH 3; the dependence on solution saturation state. *Am. J. Sci.*
903 **291**, 649-686.
904 Nordstrom D. K., Ball J. W., Donahoe R. J. and Whittemore D. (1989) Groundwater chemistry
905 and water-rock interactions at Stripa. *Geochim. Cosmochim. Acta* **53**, 1727-1740.
906 Palandri J. L. and Kharaka Y. K. (2004) A compilation of rate parameters of water-mineral
907 interaction kinetics for application to geochemical modeling. US Geological Survey.
908 Pettke T., Oberli F., Audétat A., Guillong M., Simon A. C., Hanley J. J. and Klemm L. M.
909 (2012) Recent developments in element concentration and isotope ratio analysis of
910 individual fluid inclusions by laser ablation single and multiple collector ICP-MS. *Ore*
911 *Geology Reviews* **44**, 10-38.
912 Pistiner J. S. and Henderson G. M. (2003) Lithium-isotope fractionation during continental
913 weathering processes. *Earth Planet. Sci. Lett.* **214**, 327-339.
914 Pogge von Strandmann P. A. E., Burton K. W., James R. H., van Calsteren P., Gíslason S. R. and
915 Mokadem F. (2006) Riverine behaviour of uranium and lithium isotopes in an actively
916 glaciated basaltic terrain. *Earth Planet. Sci. Lett.* **251**, 134-147.
917 Pogge von Strandmann P. A. E., Burton K. W., James R. H., van Calsteren P. and Gislason S. R.
918 (2010) Assessing the role of climate on uranium and lithium isotope behaviour in rivers
919 draining a basaltic terrain. *Chem. Geol.* **270**, 227-239.
920 Pogge von Strandmann P. A. E., Elliott T., Marschall H. R., Coath C., Lai Y.-J., Jeffcoate A. B.
921 and Ionov D. A. (2011) Variations of Li and Mg isotope ratios in bulk chondrites and
922 mantle xenoliths. *Geochim. Cosmochim. Acta* **75**, 5247-5268.
923 Pogge von Strandmann P. A. E., Porcelli D., James R. H., van Calsteren P., Schaefer B.,
924 Cartwright I., Reynolds B. C. and Burton K. W. (2014) Chemical weathering processes in
925 the Great Artesian Basin: Evidence from lithium and silicon isotopes. *Earth Planet. Sci.*
926 *Lett.* **406**, 24-36.

927 Pogge von Strandmann P. A. E. and Henderson G. M. (2015) The Li isotope response to
928 mountain uplift. *Geology* **43**, 67-70.
929 Pogge von Strandmann P. A. E., Burton K. W., Opfergelt S., Eiríksdóttir E. S., Murphy M. J.,
930 Einarsson A. and Gislason S. R. (2016) The effect of hydrothermal spring weathering
931 processes and primary productivity on lithium isotopes: Lake Myvatn, Iceland. *Chem.*
932 *Geol.* **in press**, DOI: http://dx.doi.org/10.1016/j.chemgeo.2016.02.026.
933 Polzer W. L. and Hem J. D. (1965) The dissolution of kaolinite. *J. Geoph. Res.* **70**, 6233-6240.
934 Reed M. and Palandri J. L. (2006) SOLTHERM.H06, a database of equilibrium constants for
935 minerals and aqueous species. Available from the authors, University of Oregon, Eugene,
936 USA.
937 Reesman A. L. and Keller W. D. (1968) Aqueous solubility studies of high-alumina and clay
938 minerals. *American Mineralogist* **53**, 929-&.
939 Richter F. M., Mendybaev R. A., Christensen J. N., Hutcheon I. D., Williams R. W., Sturchio N.
940 C. and Beloso Jr A. D. (2006) Kinetic isotopic fractionation during diffusion of ionic
941 species in water. *Geochim. Cosmochim. Acta* **70**, 277-289.
942 Sanjuan B., Millot R., Ásmundsson R., Brach M. and Giroud N. (2014) Use of two new Na/Li
943 geothermometric relationships for geothermal fluids in volcanic environments. *Chem.*
944 *Geol.* **389**, 60-81.
945 Sanjuan B., Millot R., Innocent C., Dezayes C., Scheiber J. and Brach M. (2016) Major
946 geochemical characteristics of geothermal brines from the Upper Rhine Graben granitic
947 basement with constraints on temperature and circulation. *Chem. Geol.* **428**, 27-47.
948 Schaltegger U. (1994) Unravelling the pre-Mesozoic history of the Aar and Gotthard massifs
949 (Central Alps) by isotopic dating — a review. *Schweizerische Mineralogische und*
950 *Petrographische Mitteilungen* **74**, 41-51.
951 Schwertmann U. (1988) Occurrence and Formation of Iron Oxides in Various
952 Pedoenvironments, in: Stucki, J.W., Goodman, B.A., Schwertmann, U. (Eds.), Iron in Soils
953 and Clay Minerals. Springer Netherlands, Dordrecht, pp. 267-308.
954 Seelig U. and Bucher K. (2010) Halogens in water from the crystalline basement of the Gotthard
955 rail base tunnel (central Alps). *Geochim. Cosmochim. Acta* **74**, 2581-2595.
956 Singleton M. J., Sonnenthal E. L., Conrad M. E., DePaolo D. J. and Gee G. W. (2005)
957 Multiphase reactive transport modeling of seasonal infiltration events and stable isotope
958 fractionation in unsaturated zone pore water and vapor at the Hanford site. *Vadose Zone J.*
959 **3**, 775-785.
960 Sonnenthal E. L., Spycher N., Apps J. A. and Simmons A. (1998) Thermo-hydro-chemical
961 predictive analysis for the drift-scale heater test. Lawrence Berkeley National Laboratory
962 report **SPY289M4**.
963 Sonnenthal E. L., Ito A., Spycher N., Yui M., Apps J. A., Sugita Y., Conrad M. E. and
964 Kawakami S. (2005) Approaches to modeling coupled thermal, hydrological and chemical
965 processes in the Drift Scale Heater Test at Yucca Mountain. *Int. J. Rock Mech. Min. Sci.*
966 **42**, 698-719.
967 Spandler C., Pettke T. and Rubatto D. (2011) Internal and External Fluid Sources for Eclogite-
968 facies Veins in the Monviso Meta-ophiolite, Western Alps: Implications for Fluid Flow in
969 Subduction Zones. *J. Petrol.* **52**, 1207-1236
970 Steefel C. I., Appelo C. A. J., Arora B., Jacques D., Kalbacher T., Kolditz O., Lagneau V.,
971 Lichtner P. C., Mayer K. U., Meussen H., Molins S., Moulton D., Parkhurst D. L., Shao H.,

Simunek J., Spycher N., Yabusaki S. and Yeh G. T. (2015) Reactive transport codes for subsurface environmental simulation. *Comput. Geosci.* **19**, 445-478.

Stober I. and Bucher K. (2015) Hydraulic conductivity of fractured upper crust: insights from hydraulic tests in boreholes and fluid-rock interaction in crystalline basement rocks. *Geofluids* **15**, 161-178.

Tardy Y., Trauth N. and Krempp G. (1972) Lithium in clay-minerals of sediments and soils. *Geochim. Cosmochim. Acta* **36**, 397-&.

Teng F.-Z., Rudnick R. L., McDonough W. F. and Wu F.-Y. (2009) Lithium isotopic systematics of A-type granites and their mafic enclaves: Further constraints on the Li isotopic composition of the continental crust. *Chem. Geol.* **262**, 370-379.

Trotignon L., Beaucaire C., Louvat D. and Jean-François A. (1999) Equilibrium geochemical modelling of Äspö groundwaters: a sensitivity study of thermodynamic equilibrium constants. *Appl. Geochem.* **14**, 907-916.

Verney-Carron A., Vigier N., Millot R. and Hardarson B. S. (2015) Lithium isotopes in hydrothermally altered basalts from Hengill (SW Iceland). *Earth Planet. Sci. Lett.* **411**, 62-71.

Vigier N., Decarreau A., Millot R., Carignan J., Petit S. and France-Lanord C. (2008) Quantifying Li isotope fractionation during smectite formation and implications for the Li cycle. *Geochim. Cosmochim. Acta* **72**, 780-792.

Vigier N., Gislason S. R., Burton K. W., Millot R. and Mokadem F. (2009) The relationship between riverine lithium isotope composition and silicate weathering rates in Iceland. *Earth Planet. Sci. Lett.* **287**, 434-441.

Vigier N. and Goddéris Y. (2015) A new approach for modeling Cenozoic oceanic lithium isotope paleo-variations: the key role of climate. *Clim. Past* **11**, 635-645.

Waber H. N., Gimmi T. and Smellie J. A. T. (2012) Reconstruction of palaeoinfiltration during the Holocene using porewater data (Laxemar, Sweden). *Geochim. Cosmochim. Acta* **94**, 109-127.

Wanner C. and Sonnenthal E. L. (2013) Assessing the control on the effective kinetic Cr isotope fractionation factor: A reactive transport modeling approach. *Chem. Geol.* **337**, 88-98.

Wanner C., Sonnenthal E. L. and Liu X.-M. (2014) Seawater d7Li a direct proxy for global CO2 consumption by continental silicate weathering? *Chem. Geol.* **381**, 154-167.

Wanner C., Druhan J., Amos R., Alt-Epping P. and Steefel C. (2015) Benchmarking the simulation of Cr isotope fractionation. *Comput Geosci* **19**, 497-521.

Wimpenny J., Gislason S. R., James R. H., Gannoun A., Pogge Von Strandmann P. A. E. and Burton K. W. (2010) The behaviour of Li and Mg isotopes during primary phase dissolution and secondary mineral formation in basalt. *Geochim. Cosmochim. Acta* **74**, 5259-5279.

Wolery T. J. (1992) *EQ3/6: Software package for geochemical modeling of aqueous systems: Package overview and installation guide (version 7.0)*, Livermore, California.

Wunder B., Meixner A., Romer R. and Heinrich W. (2006) Temperature-dependent isotopic fractionation of lithium between clinopyroxene and high-pressure hydrous fluids. *Contrib. Mineral. Petr.* **151**, 112-120.

Xu T., Sonnenthal E. L., Spycher N. and Zheng L. (2014) TOUGHREACT V3.0-OMP Reference Manual: A Parallel Simulation Program for Non-Isothermal Multiphase Geochemical Reactive Transport. *LBNL Manual*

http://esd.lbl.gov/FILES/research/projects/tough/documentation/TOUGHREACT_V3-OMP_RefManual.pdf.

Yang L. and Steefel C. I. (2008) Kaolinite dissolution and precipitation kinetics at 22°C and pH 4. *Geochim. Cosmochim. Acta* **72**, 99-116.

Zhang L., Chan L.-H. and Gieskes J. M. (1998) Lithium isotope geochemistry of pore waters from ocean drilling program Sites 918 and 919, Irminger Basin. *Geochim. Cosmochim. Acta* **62**, 2437-2450.

Table

Table 1: Simulated mineral dissolution and precipitation reactions

Mineral phase	[a]log(K) T=25°C	[a]log(K) T=60°C	[b]k_{25}^{n} (mol/m^2/s)	[b]E_a^{n} (kJ/mol)	[b]k_{25}^{ac} (mol/m^2/s)	[b]E_a^{ac} (kJ/mol)	[b]m_{ac}	[b]k_{25}^{ba} (mol/m^2/s)	[b]E_a^{ba} (kJ/mol)	[b]m_{ba}	Hydrolysis reaction (written with primary species)
Albite	1.4	0.3	2.75e-13	69.8	6.92e-11	65.0	0.457	2.51e-16	71.0	-0.57	$NaAlSi_3O_8 + 4H^+ = Na^+ + 3SiO_{2(aq)} + Al^{3+} + 2H_2O$
Orthoclase	-0.5	-1.3	3.89e-13	38.0	8.71e-11	51.7	0.50	6.31e-22	94.1	-0.82	$KAlSi_3O_8 + 4H^+ = K^+ + 3SiO_{2(aq)} + Al^{3+} + 2H_2O$
Quartz	-4.0	-3.5	4.57e-14	90.1	6.92e-30	65.0	0.457	[d]1.00-14	[d]0.0	-0.5	$SiO_{2(s)} = SiO_{2(aq)}$
Annite[c1]	29.4	24.2	2.82e-13	22.0	-	-	-	-	-	-	$KFe_3AlSi_3O_{10}(OH)_2 + 10H^+ = Al^{3+} + K^+ + 3Fe^{2+} + 6H_2O + 3SiO_2$
Phlogopite[c1,e]	37.4	31.5	2.82e-13	22.0	-	-	-	-	-	-	$K_{1.026}Mg_{2.974}Li_{0.026}AlSi_3O_{10}(OH)_2 + 10H^+ = Al^{3+} + K^+ + 3Mg^{2+} + 6H_2O + 3SiO_2 + 0.00199\ ^6Li^+ + 0.02401\ ^7Li^+$
Muscovite	8.7	4.62	1.0e-13	22.0	-	-	-	-	-	-	$KAl_2AlSi_3O_{10}(OH)_2 + 10H^+ = 3Al^{3+} + K^+ + 6H_2O + 3SiO_2$
Chamosite[c2]	41.1	32.9	3.02e-13	88.0	-	-	-	-	-	-	$(Fe)_5Al(AlSi_3O_{10})(OH)_8 + 16H^+ = 5Fe^{2+} + 2Al^{3+} + 3SiO_2 + 12\ H_2O$
Clinochlore[c2]	55.9	46.0	3.02e-13	88.0	-	-	-	-	-	-	$(Mg)_5Al(AlSi_3O_{10})(OH)_8 + 16H^+ = 5Mg^{2+} + 2Al^{3+} + 3SiO_2 + 12\ H_2O$
Kaolinite[c3]	3.2	0.7	1.98e-13	22.2	-	-	-	-	-	-	$Al_2Si_2O_5(OH)_4 + 6H^+ = 2Al^{3+} + 2SiO_{2(aq)} + 5H_2O$
$^6Li_{kaolinite}$[c3]	-4.9409764	-4.9409764	1.98e-13	22.2	-	-	-	-	-	-	$^6Li = {}^6Li^+$
$^7Li_{kaolinite}$[c3]	-4.9187	-4.9187	1.98e-13	22.2	-	-	-	-	-	-	$^7Li = {}^7Li^+$
Pyrite	217.4	191.1	2.80e-5	56.9	-	-	-	-	-	-	$FeS_2 + H_2O + 3.5\ O_{2(aq)} = Fe^{2+} + 2SO_4^{2-} + 2H^+$
Calcite	1.8	1.3	1.55e-6	23.5	-	-	-	-	-	-	$CaCO_3 + H^+ = HCO_3^- + Ca^{2+}$
Li-source[f]	[f]	[f]	[f]	[f]	-	-	-	-	-	-	$Li_{0.04}Na_{0.96}Cl = 0.00305\ ^6Li^+ + 0.03695\ ^7Li^+ + 0.96Na^+ + Cl^-$
Secondary species	$AlOH^{2+}$, $Al(OH)_2^+$, $HAlO_2$, AlO_2^-, $KAlO_2$, $NaAlO_2$, $AlSO_4^+$, $Al(SO_4)_2^-$, $CO_{2(aq)}$, CO_3^{2-}, $CaCO_{3(aq)}$, $CaHCO_3^+$,$CaCl^+$, $CaCl_2$, $CaOH^+$, $CaSO_4$, HCl, $FeCl^+$, FeC_{l2}, FeO, $FeOH^+$, $HFeO_2$, $FeSO_4$, KCl, $KHSO_4$, KOH, KSO_4^-, $MgCO_3$, $MgHCO_3^+$, $MgCl^+$, $MgOH^+$, $MgSO_4$, NaCl, NaOH, $NaCO_3^-$, $NaHCO_3$, $NaSO_4^-$, OH^-, HSO_4^-, HS^-, S^{2-}, $H_2S_{(aq)}$, $HSiO_3^-$, $H_2SiO_4^{2-}$, $CaHSiO_3^+$, $MgHSiO_3^+$, $NaHSiO_3$										

[a] equilibrium constants log(*K*) were defined according to the Soltherm.H06 database (Reed and Palandri, 2006). The temperature dependence is calculated according to $\log(K)_{T[K]} = a*\ln(T_K) + b + c*T_K + d/T_K + e/T_K^2$. a,b,c,d and e are constants defined in the database. For the listed mineral phases, however, the interpolation between 25 and 60°C is almost linear.

[b] Reaction rate constants k, activation energies E_a and rate dependence on ph (m_{ac} and m_{ba}) were defined according to Palandri & Kharaka (2006)

[cx] Endmbember of solid solution x.

[d] A constant value for k_{25}^{ba} of 1e-14 refers to a temperature of ca. 65°C according to equation 3 and taking into account an activation energy of 108366 (Palandri & Kharaka, 2006). A rate constant slightly higher than proposed in the Palandri & Kharaka (2006) compilation was required to get quartz solubility controlled SiO_2 concentrations such as observed for our water samples (Bucher et al., 2012).

[e] Corresponds to a phlogopite Li concentration of 217 ppm to get an initial bulk rock Li conc. of 8.8 µg/g (Table 2) (at a phlogopite vol. fraction of 0.02), and a δ^7Li value of 1.7‰.

[f] Hypothetical solid phase defined to simulated a porewater or unknown mineral Li source with a δ^7Li value of 8.7‰. Corresponding parameters are given in the text for each scenario.

- No pH dependence of the rate constant considered at acidic and/or basic conditions

Table 2:
Solid Li concentration measurements performed using AAS for bulk rock concentrations and laser ablation ICP-MS for individual mineral phases

		Mineral stoichiometry[a]	Li (µg/g)[b]	Stdv. (1ε)	N[c]	Mg/Li
Bristner Granite	Plagioclase	$NaAlSi_3O_8$	2.1	±1.1	7	1-3
	K-Feldspar	$KAlSi_3O_8$	2.4	±1.6	2	<1
	Quartz	SiO_2	4.4	±0.9	3	<1
	chloritized biotite	$K_{0.5}Fe_{3-3.5}Al_{<1}(AlSi_3O_{10}(OH)_{5-8}$	464	±90	2	4
	[e]Muscovite	$KAl_2(AlSi_3O_{10})(OH)_8$	462	±53	4	2
	bulk rock		6.1	±0.2	2	3
BuMigIII	[d]Plagioclase	$NaAlSi_3O_8$	7.7	±5.1	10	25-35
	K-Feldspar	$K_{0.6}Na_{0.4}AlSi_3O_8$	45	-	1	35
	Quartz	SiO_2	<0.1	-	3	-
	chloritized biotite	$K_{0.03-0.3}(Mg,Fe)_{2-3}Al_{<1}(AlSi_3O_{10}(OH)_{2-8}$	217	±32	5	65-85
	[d]Muscovite			-	10	-
	bulk rock		8.8	-	1	138

[a]Inferred stoichiometry based on the full chemical composition of the specific mineral phases lis isted in the electronic appendix
[b]Concentrations refer to average concentrations obtained from N measurements and are derived from ^7Li measurements (see electronic appendix) taking into account the bulk earth Li isotope abundance.
[c]Number of measurements performed on specific mineral phases
[d]In case of BuMigIII, plagioclase is heavily altered to sericitic muscovite. Also, muscovite is too small to perform individual measurements. Accordingly, plagioclase measurements including the reported Mg/Li value also contain a muscovite component .
[e]Muscovite measurements for the Bristner Granite refer to a mixture between chloritized biotite and muscovite

Table 3: Aqueous δ^7Li and Li concentration measurements (this study) and major species concentrations reported by Bucher et al. (2012)

	Sample	Tunnel meter	Over-burden (m.a.t)	Temp (°C)	pH	Flow rate (L/s)	Li^+ (mg/L)	δ^7Li (‰)	Ca^{2+} (mg/L)	Mg^{2+} (mg/L)	Na^+ (mg/L)	K^+ (mg/L)	Fe (mg/L)	Al (mg/L)	[a]C(4) as HCO_3^- (mg/L)	SO_4^{2-} (mg/L)	Cl^- (mg/L)	F^- (mg/L)	SiO_2 (mg/L)	Mg/Li (mol ratio)	Cl/Li (mol ratio)
Bristner Granite	A005	8509	320	22.0	9.11	0.10	1.62	8.6±0.2[b]	1.8	0.1	251	10.0	0.27	0.747	264	93	155	19.0	18.9	0.01	18.6
	A038	8566	315	24.2	9.03	0.002	1.60	8.5±0.0	5.2	0.1	266	11.6	<0.02	0.101	318	82	149	23.8	24.2	0.01	18.1
	A042	8903	350	25.1	8.67	0.04	3.09	9.0±0.2	3.7	0.2	511	17.2	<0.02	0.016	395	216	386	27.2	24.0	0.02	24.3
	A035	8381	345	21.5	8.74	0.00	2.60	8.6±0.2	3.0	0.2	405	9.9	0.35	<0.01	371	157	297	27.6	19.1	0.03	22.3
	A039	8575	305	21.4	8.78	0.15	2.86	9.0±0.5	3.0	0.1	461	13.9	<0.02	0.024	314	187	350	26.8	17.8	0.01	23.8
	A043	8920	350	24.1	8.70	0.03	3.23	9.1±0.2	3.0	0.2	499	17.3	0.07	0.012	365	214	387	26.6	20.1	0.02	23.3
	A037	8432	325	21.5	8.91	0.01	2.16	8.5±0.4	1.9	0.1	348	12.5	<0.02	0.008	310	129	242	26.9	22.8	0.01	21.8
	A007	8611	325	21.9	8.89	0.01	2.10	8.5±0.7	1.6	0.1	311	10.3	0.18	0.392	316	116	213	24.4	18.9	0.01	19.7
	A041	8737	330	22.1	8.73	0.10	3.06	9.0±0.2	3.3	0.2	512	15.6	<0.02	0.054	354	213	383	27.1	22.9	0.02	24.4
BuMigIII	A099	14850	1975	42.6	9.40	0.02	0.013	14.8±0.3	5.6	<0.1	26.1	0.9	<0.02	0.093	11.0	40	1.2	1.6	28.2	<2.1	17.4
	A100	14951	2050	43.7	9.31	0.07	0.014	10.7±0.5	5.2	<0.1	26.6	0.7	<0.02	0.135	13.9	40	0.8	1.6	28.2	<2.0	10.5
	A102	14986	2090	43.4	9.47	0.20	0.013	19.7±0.1	5.5	<0.1	25.0	0.5	<0.02	0.098	13.5	36	0.7	1.7	23.3	<2.2	11.1
	A029	15095	2100	42.8	9.80	2.50	0.010	41.1±0.6	9.0	0.5	30.2	1.2	1.03	0.033	13.9	38	1.2	3.1	30.7	13.7	24.3
	A103	15106	2095	36.7	8.29	0.01	0.016	22.3±0.1	13.5	0.2	26.8	1.5	0.29	0.641	68.0	31	2.6	1.8	30.2	4.0	32.5
	A104	15136	2090	43.4	9.36	0.15	0.017	17.4±0.3	11.0	<0.1	27.5	0.8	<0.02	0.077	13.1	54	1.2	3.9	28.3	<1.7	13.9
	A027	14794	1920	43.0	9.44	0.02	0.012	27.2±0.4	5.0	<0.1	26.6	0.9	<0.02	0.094	9.1	39	0.8	1.6	32.2	<2.4	13.1
	A126	15334	2035	43.2	9.27	0.02	0.054	17.9±0.1	412.0	<0.1	86.1	1.4	0.31	0.042	17.7	1189	7.8	2.6	26.6	<0.5	25.2

[a]In case of BuMigIII HCO_3^- concentrations were calculated to maintain charge balance
[b]2σ uncertainty

Table 4: Saturation indices of selected primary and secondary minerals calculated using TOUGHREACT in conjunction with the Soltherm.H06 database (Reed and Palandri, 2006)

	Sample	pH	Quartz	Chalce-dony	Orthoclase	Albite	Calcite	Anhydrite	Kaolinite (Soltherm.H06)[a]	Kaolinite (EQ3/6)[a]	Gibbsite	$Al(OH)_{3\ (am)}$	Illite	log f_{CO2}
Bristner Granite	A005	9.11	0.41	0.09	3.64	3.35	0.15	-3.59	6.83	4.13	1.69	-1.96	4.33	-3.74
	A038	9.03	0.54	0.22	3.22	2.89	0.61	-3.19	5.51	2.80	0.90	-2.75	2.90	-3.57
	A042	8.67	0.60	0.28	2.73	2.51	0.16	-3.02	4.71	2.00	0.45	-3.21	1.81	-3.12
	A035	8.74	0.50	0.17	0.42	0.34	0.14	-3.19	0.83	-1.87	-1.39	-5.05	0.81	-3.21
	A039	8.78	0.45	0.13	2.37	2.20	0.09	-3.15	4.55	1.85	0.52	-3.14	1.49	-3.33
	A043	8.70	0.52	0.20	2.36	2.13	0.07	-3.11	4.24	1.53	0.29	-3.36	1.21	-3.18
	A037	8.91	0.54	0.22	2.13	1.88	0.04	-3.45	3.53	0.82	-0.08	-3.74	0.50	-3.46
	A007	8.89	0.47	0.15	3.53	3.32	-0.05	-3.57	6.81	4.11	1.63	-2.03	4.14	-3.43
	A041	8.73	0.56	0.24	3.12	2.94	0.13	-3.07	5.58	2.87	0.91	-2.74	2.81	-3.23
BuMigIII	A099	9.40	0.08	-0.22	0.25	0.11	-0.01	-2.97	1.95	-0.55	-0.46	-3.83	-1.77	-5.34
	A100	9.31	0.13	-0.17	0.40	0.42	-0.02	-3.00	2.54	0.05	-0.21	-3.58	-1.22	-5.14
	A102	9.47	-0.04	-0.34	-0.41	-0.25	0.12	-3.03	1.61	-0.89	-0.51	-3.88	-2.42	-5.34
	A029	9.80	-0.15	-0.45	-0.78	-0.98	0.54	-2.83	-0.22	-2.71	-1.31	-4.69	-3.86	-5.77
	A103	8.29	0.51	0.20	2.72	2.35	0.04	-2.78	7.21	4.65	1.75	-1.70	3.66	-3.41
	A104	9.36	0.10	-0.20	0.13	0.11	0.30	-2.58	1.90	-0.60	-0.51	-3.88	-1.91	-5.23
	A027	9.44	0.12	-0.19	0.33	0.23	-0.10	-3.02	1.95	-0.55	-0.50	-3.87	-1.70	-5.47
	A126	9.27	0.09	-0.22	-0.03	-0.33	1.29	-0.26	1.42	-1.08	-0.73	-4.10	-2.56	-5.34

[a] To discuss the possible precipitation of kaolinite, the saturation index was calculated using log(K) values tabulated in the EQ3/6 database (Wolery et al., 1992) in addition to the ones tabulated in the Soltherm database (Table 1, Reed and Palandri, 2006).

Table 5: Initial and boundary conditions defined for performing reactive transport model simulations.

		Initial condition	Boundary condition (infiltrating fluid)
Temperature	°C	variable	10
pH	-	5.67	5.67
C(4) as HCO_3^-	mol/kgH_2O	1.5e-5	1.5e-5
Na^+	mol/kgH_2O	1.0e-10	1.0e-10
K^+	mol/kgH_2O	1.0e-10	1.0e-10
Mg^{2+}	mol/kgH_2O	1.0e-10	1.0e-10
Ca^{2+}	mol/kgH_2O	1.0e-10	1.0e-10
Al^{3+}	mol/kgH_2O	1.0e-10	1.0e-10
Li^+	mol/kgH_2O	1.0e-10	1.0e-10
$SiO_{2(aq)}$	mol/kgH_2O	1.0e-10	1.0e-10
$O_{2(aq)}$	mol/kgH_2O	3.86e-4	3.86e-4
Fe^{2+}	mol/kgH_2O	1.0e-10	1.0e-10
[b]Albite	vol frac (of solids)	0.31	0.0
Orthoclase	vol frac (of solids)	0.03	0.0
Quartz	vol frac (of solids)	0.48	0.0
[a1]Annite	vol frac (of solids)	0.02	0.0
[a1]Phlogopite	vol frac (of solids)	0.02	0.0
Muscovite	vol frac (of solids)	0.1	0.0
[a2]Chamosite	vol frac (of solids)	0.0075	0.0
[a2]Clinochlore	vol frac (of solids)	0.0075	0.0
Pyrite	vol frac (of solids)	0.01	0.0
Calcite	vol frac (of solids)	0.01	0.0
Kaolinite [a3]	vol frac (of solids)	0.0	0.0
$^6Li_{kaolinite}$ [a3]	vol frac (of solids)	0.0	0.0
$^7Li_{kaolinite}$ [a3]	vol frac (of solids)	0.0	0.0
Porosity	-	0.01	1.0

[ax]end-member of solid solution x
[a]Specified nineralogical composition is based on XRF analyses performed on BuMigIII (Seelig and Bucher, 2010) as well as on laser ablation ICP-MS measurements (electronic appendix).

Table 6: Parameters chosen for the various model runs

Scenario	Scenario #	Max $[Li]_{kaolinite}$ (ppm)	*$k_{kaolinite}$	$\varepsilon_{kaolinite}$	$\delta'Li_{Li0.04Na0.96Cl}$ (‰)	Li influx location (m)
Continuous Li influx	C1	75	base case	-50	8.7	-
Mixing scenario (single point Li influx)	M1	25	base case	-50	8.7	-400
	M2	50	base case	-50	8.7	-400
	M3	75	base case	-50	8.7	-400
	M4	75	base case	-37.5	8.7	-400
	M5	75	base case	-25	8.7	-400
	M6	75	base case x 2/3	-50	8.7	-400
	M7	75	base case x 1/3	-50	8.7	-400
	M8	75	base case	-50	8.7	-200
	M9	75	base case	-50	8.7	-1200
	M10	50	base case	-50	1.7	-400

*base case: k_{25}=1.98e-13 (Table 1)

Figure

Figure 1: Geological cross section through the Amsteg section of the Gotthard rail base tunnel. The two sections from which water and rock samples were taken for Li concentration and Li isotope measurements are highlighted (Bristner Granite and BuMigIII) (modified from Bucher et al., 2012).

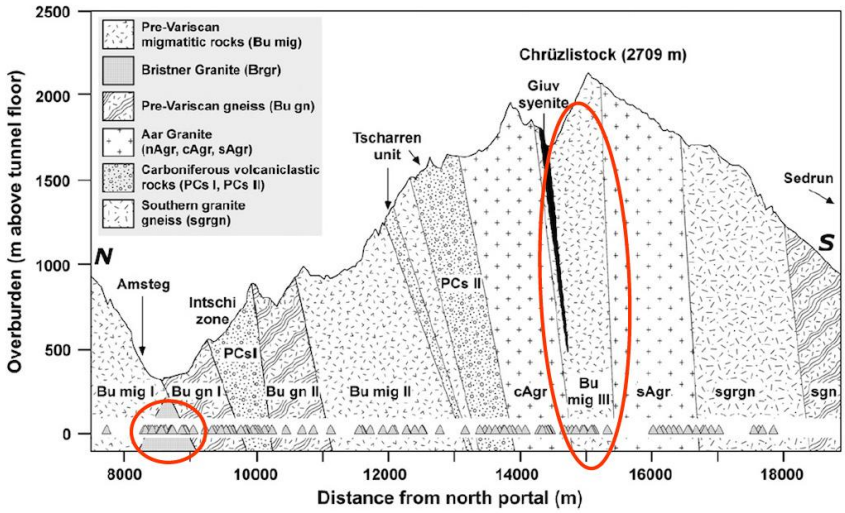

Figure 2: δ^7Li values of BuMigIII water samples plotted against the pH (**a**), the [Li] (**b**), and the molar Li/Na ratio (**c**).The shown correlations were obtained by not considering the two samples with special features (e.g., anhydrite dissolution and low temperature). **d** Rayleigh model.The Rayleigh model shown in **(d)** ($\delta^7Li = \delta^7Li_{Ini}+1000)f^{\alpha-1})-1000$) was obtained using an enrichment factor ε of -50‰ (ε=(α-1)*1000), an initial δ^7Li of 7‰ and a [Li] of 17 µg/L at f=1.

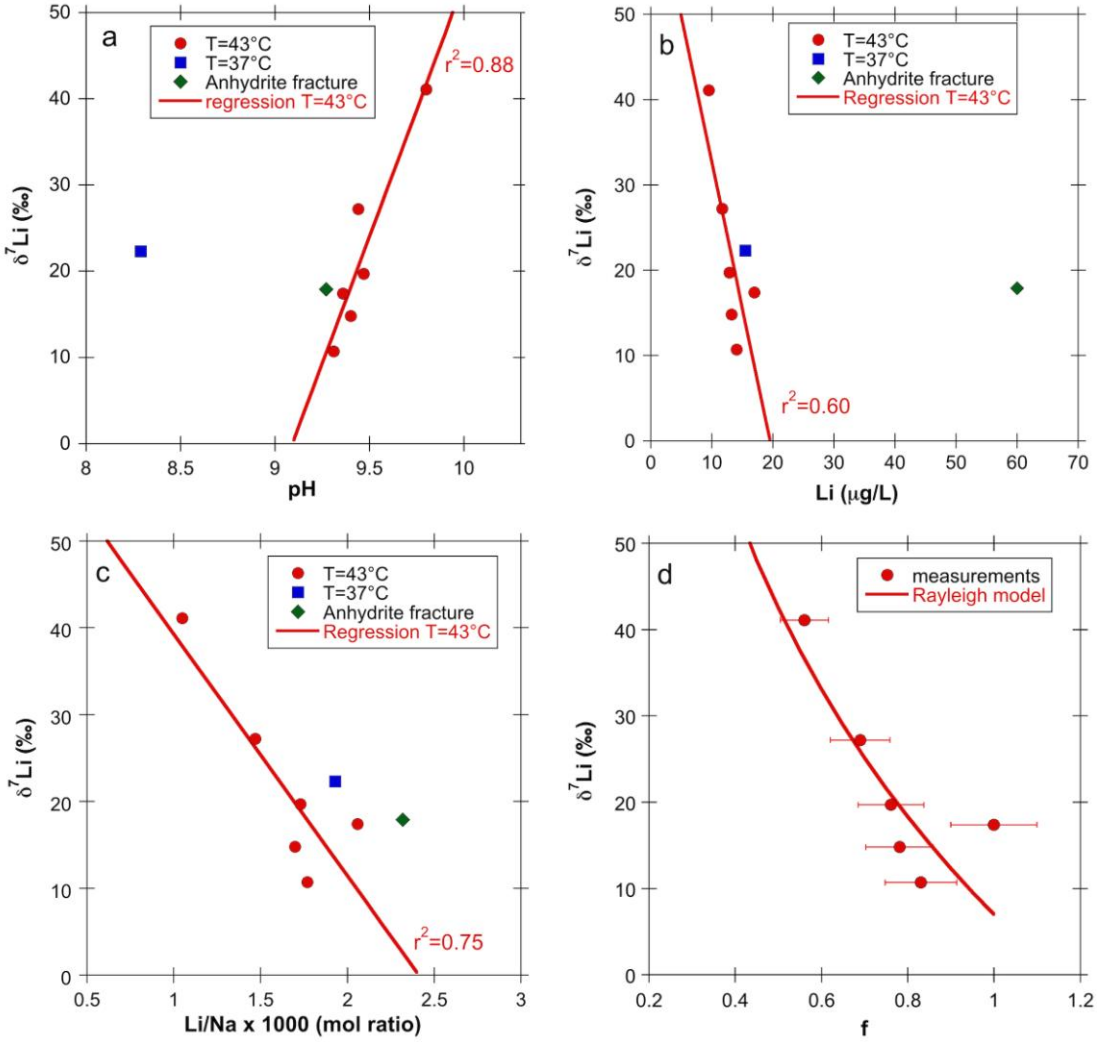

Figure 3: Excellent linear correlation between Li^+ and Cl^- observed for groundwater samples collected from the Bristner Granite.

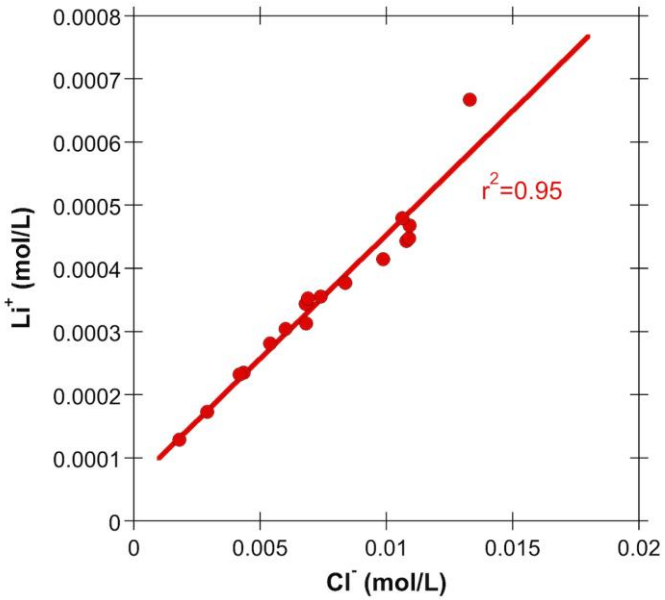

Figure 4: Comparison between experimentally determined and tabulated log(K) values for the following kaolinite hydrolysis reaction: $Al_2Si_2O_5(OH)_4 + 3H_2O = 2Al(OH)_4^- + 2SiO_2 + 2H^+$.

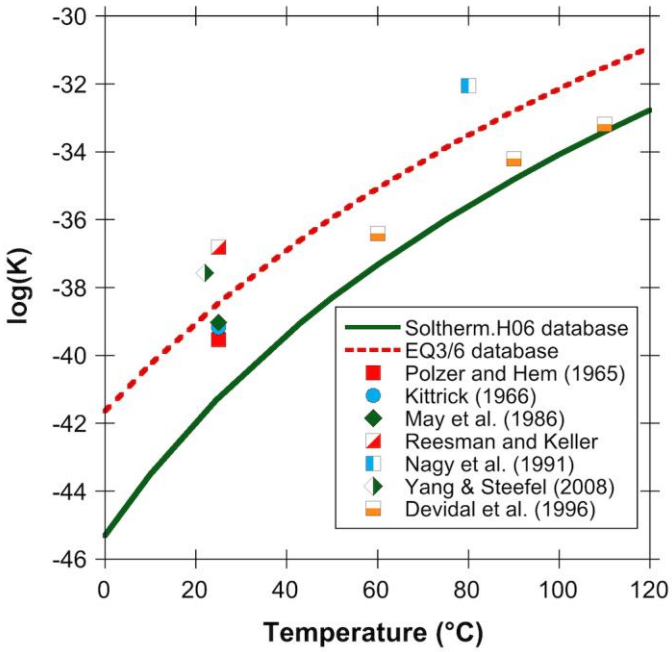

Figure 5: Li influx scenarios and corresponding model setups for simulating the infiltration of meteoric water into the BuMigIII rock column above the tunnel.

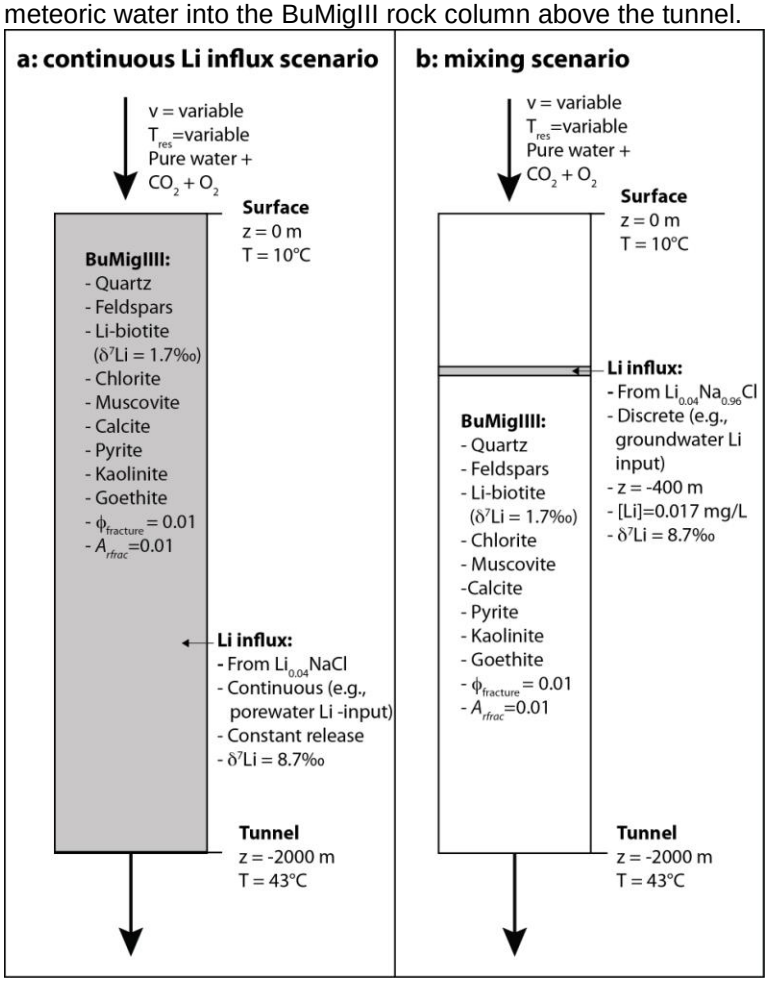

Figure 6: General behaviour of the simulated interaction between infiltrating meteoric water and the granitic BuMigIII. Steady state profiles along the model are shown for temperature and pH (**a)**, total major species concentrations (**b**), changes in mineral volume fractions relative to t=0 after a simulated time of 10'000 years (**c**), and saturation indices of selected mineral phases (**d)** and refer to a general situation where chemical equilibrium is approached along the flow path (e.g., v=1 m/year and A_{rfrac}=0.01 $m^2/m^3_{fractured\_medium}$)

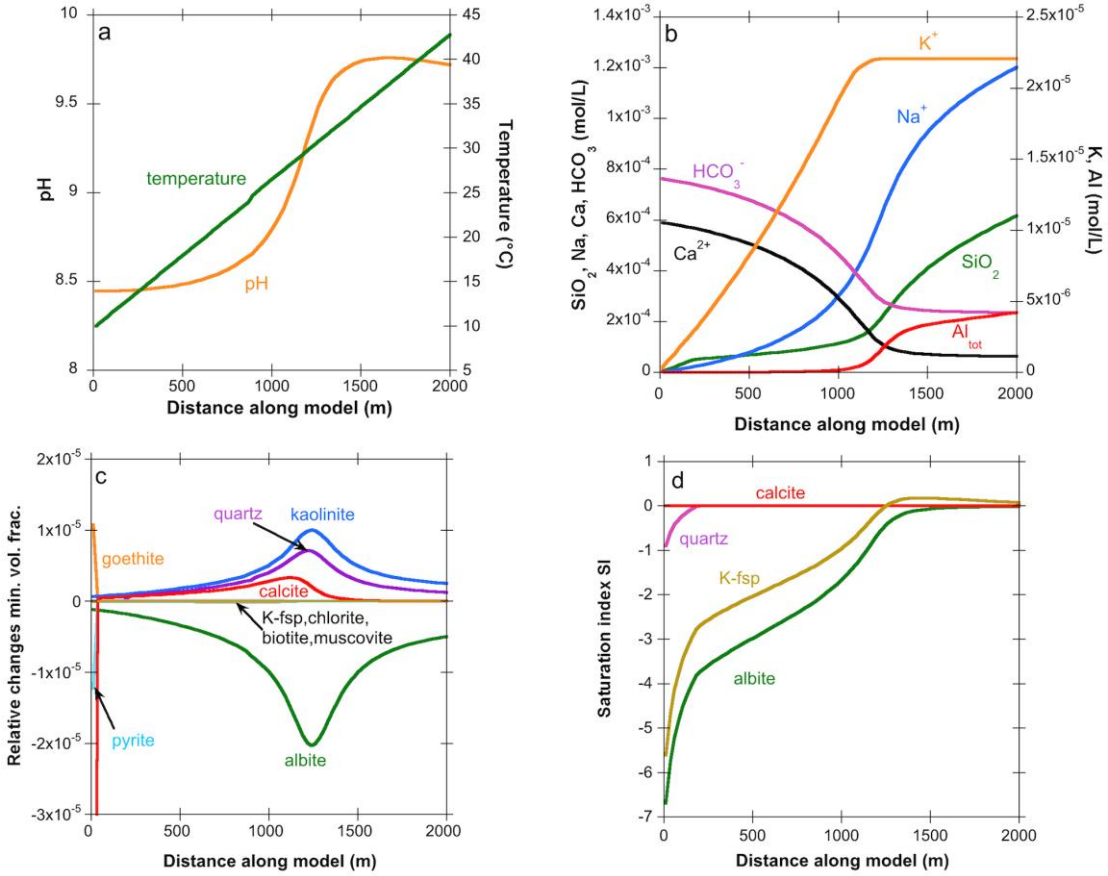

Figure 7: General behavior of Li in the two Li influx scenarios (Fig. 5) at the same reaction progress as shown in Fig. 6. (**a**) continuous Li influx sceneario. (**b**) mixing scenario. (**c**) correlation between δ^7L and Li. Results correspond to an Li isotope enrichment and maximum amount of Li in kaolinite of -50‰ and 25 µg/g, respectively (simulations C1 and M3, Table 6).

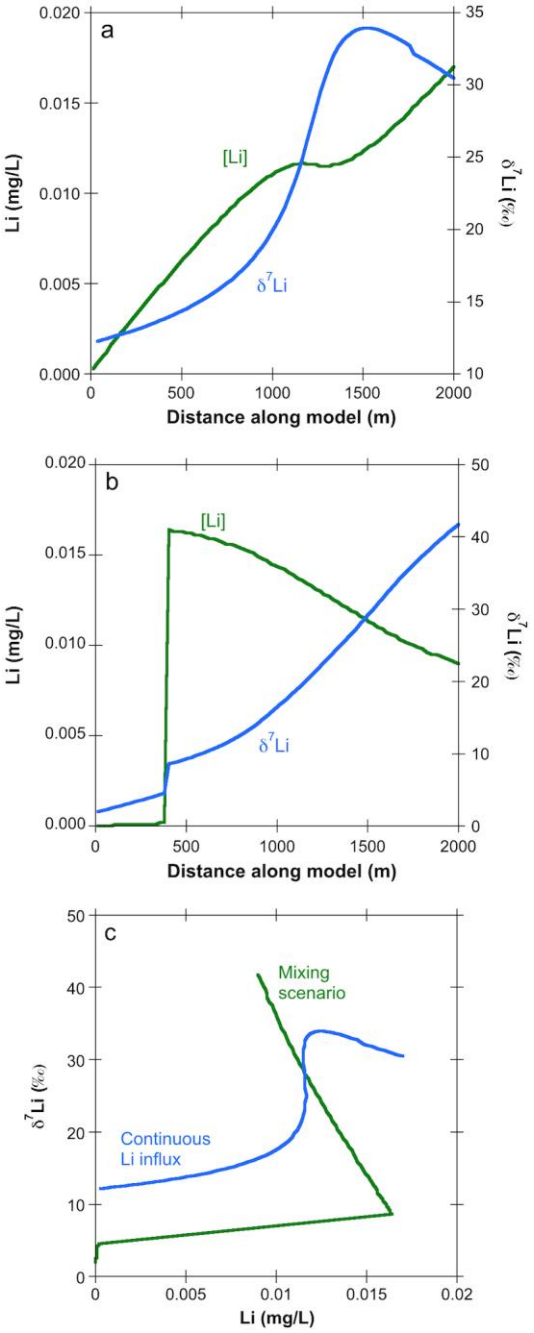

Figure 8: Major species concentrations computed for the tunnel level and plotted against the pH to illustrate their behavior with respect to a variable reaction progress along the model domain (e.g., variable residence time). Also shown are corresponding measurements of BuMigIII groundwater samples.

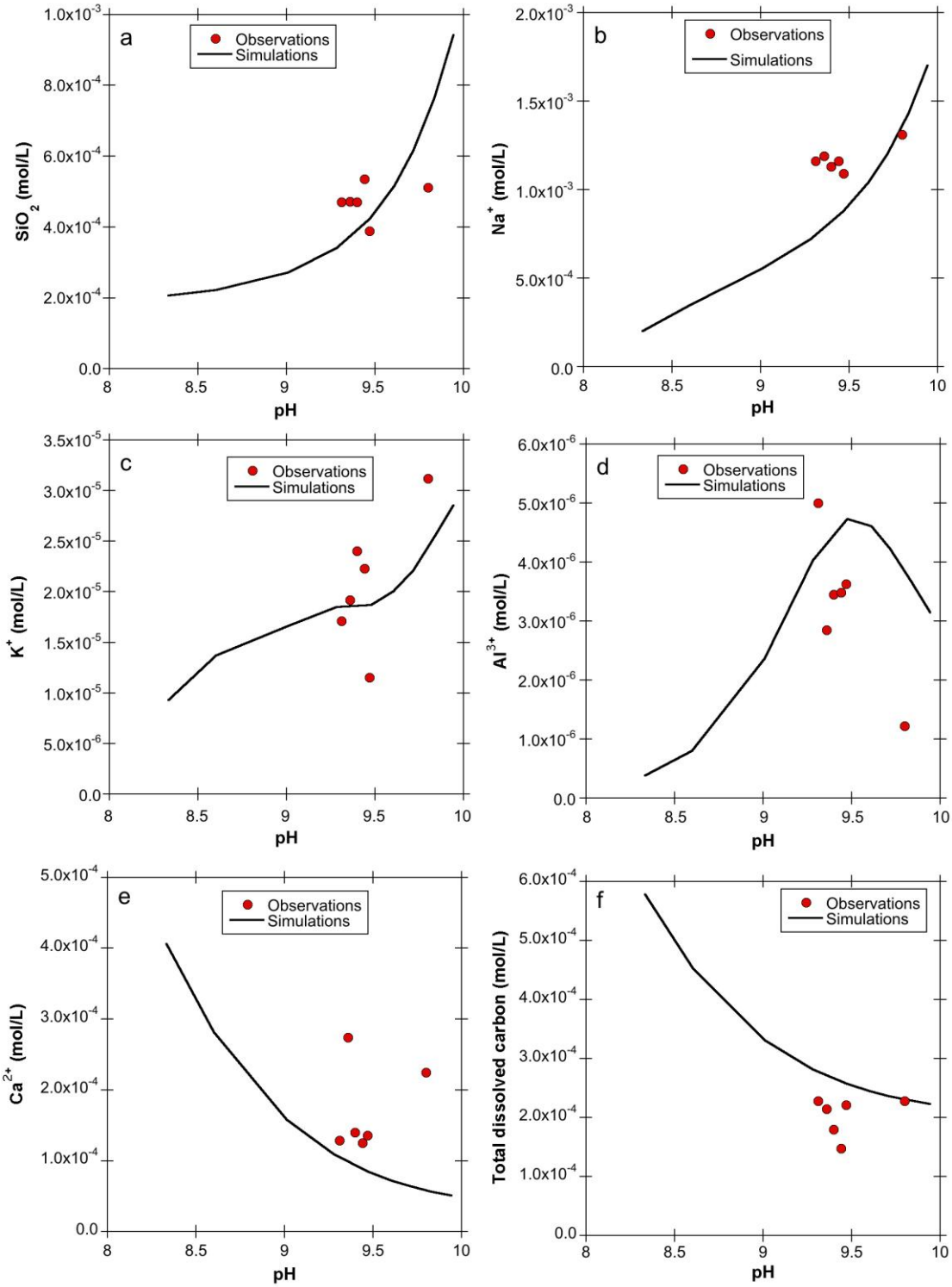

Figure 9: Sensitivity analyses performed for the mixing scenario (Fig. 5b). (**a)** compares measured δ^7Li and [Li] with values computed as a function of the reaction progress along the model domain (i.e., as a function of pH/residence time) and for a variable maximum Li concentration in kaolinite (simulations M1-M3, Table 6). (**b)** shows the same parameters as in **a,** but for a varying Li isotope enrichment factor (simulations M3-M5). In (**c)** the comparison between model and observations is shown for a varying kaolinite precipitation rate (simulations M3,M6,M7).

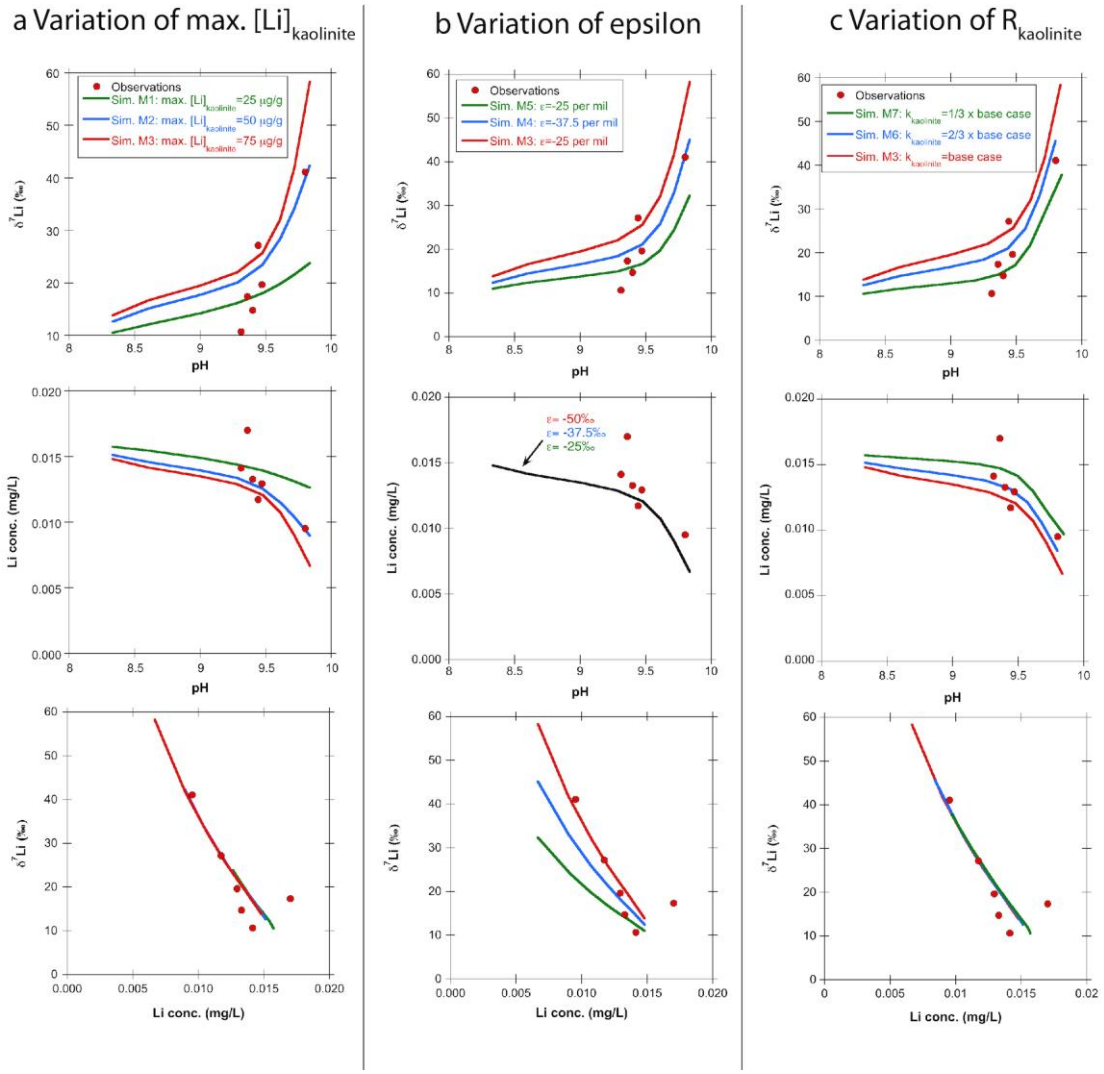

Fig. 10. Two parameter combinations (simulation M7 and M10, Table 6) that can well approximate the correlations between δ^7Li, Li and pH observed in the BuMigIII groundwater when running the model for a variable reaction progress (e.g., by varying the residence time).

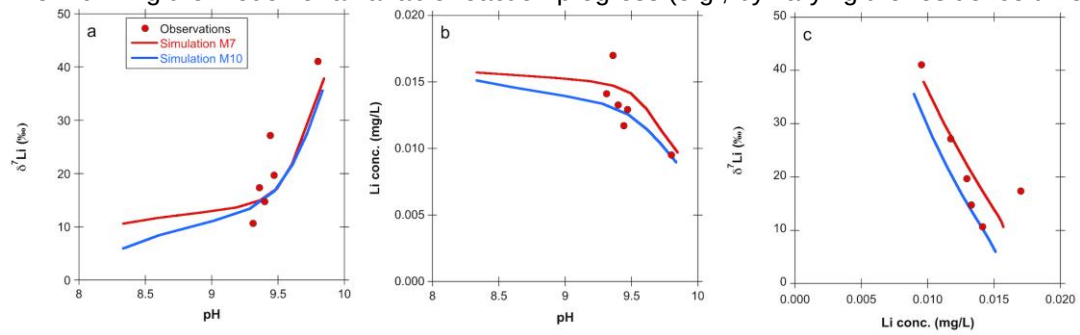

Figure 11: Sensitivity of δ^7Li values on the aqueous Li concentration. Computed Li concentration (a) and δ^7Li (b) at the tunnel level are shown for a varying Li concentration of the simulated groundwater mixture (Fig. 5b) as a function of the reaction progress (i.e., pH).